GREEN LIGHT EMITTING DIODES AND LASER DIODES

GROWN BY METALORGANIC CHEMICAL VAPOR DEPOSITION

A Master Thesis
Presented to
The Academic Faculty

by

Zachary M. Lochner

In Partial Fulfillment
of the Requirements for the Degree
Master of Science in the
School of Electrical and Computer Engineering

Georgia Institute of Technology
May 2010

GREEN LIGHT EMITTING DIODES AND LASER DIODES

GROWN BY METALORGANIC CHEMICAL VAPOR DEPOSITION

Approved by:

Dr. Russell Dupuis, Advisor
School of Electrical and Computer Engineering
Georgia Institute of Technology

Dr. Shyh-Chiang Shen
School of Electrical and Computer Engineering
Georgia Institute of Technology

Dr. Abdallah Ougazzaden
School of Electrical and Computer Engineering
Georgia Institute of Technology

Date Approved: 4 April 2010

ACKNOWLEDGEMENTS

I would like to express my thanks to everyone who made this work possible. First and foremost, I am grateful to my advisor, Dr. Russell Dupuis, for providing me with the valuable opportunity to work in the Advanced Materials and Devices Group. His advice, expertise on MOCVD, and the resources he has provided me are unparalleled in most other graduate programs. I am very fortunate to be a part of his research group.

I would like to thank my colleagues in AMDG, notably Dr. Jae-Hyun Ryou, our invaluable research engineer who is always happy to lend on a hand on any of the numerous technical/personal issues that come up in the life of a researcher; Dr. Jianping Liu, with whom I worked closely on the work presented here; Dr. Hee Jin Kim and Suk Choi, close friends whom also began at Georgia Tech in the Fall of 2007; Yong Huang a fellow grad student who is always good at lifting the mood; and Andrea Cooper, who does a fantastic job as our group administrator. I must also take time to thank two students who came before me: Dr. Dongwon Yoo and Dr. Jae Boum Limb, both of whom graduated right before I arrived, but their work in the AMDG paved the way for the results presented here.

My gratitude is also extended to our collaborating professor on the laser project and thesis committee member, Dr. Shyh-Chiang Shen, and his students, particularly Yun Zhang, for the wonderful work they have done on fabrication development. I am also gracious to Dr. Abdallah Ougazzaden for kindly agreeing to serve on my reading committee. These projects were made possible with generous financial support from the

Department of Energy, DARPA, and the Steve W. Chaddick Endowed Chair in Electro-Optics at the Georgia Institute of Technology.

Finally, my loving thanks go to my family. My parents, Tom Lochner and Joan Meyer, taught me the values of academic excellence and hard work. They always trusted me to make the right decisions and supported whatever those may be, and it has worked out well. I am also grateful for my sister, Claire Lochner, whom I somehow convinced to follow in my footsteps as an Electrical Engineer. Whatever the reason, she makes me very proud.

TABLE OF CONTENTS

LIST OF FIGURES

SUMMARY

This thesis describes the development of III-nitride materials for light emitting applications. The goals of this research were to create and optimize a green light emitting diode (LED) and laser diode (LD). Metalorganic chemical vapor deposition (MOCVD) was the technique used to grow the epitaxial structures for these devices. Several measurement techniques were employed to characterize these structures such as x-ray diffraction, atomic force microscopy, Hall-effect measurement, photoluminescence, electroluminescence, and secondary ion mass spectrometry, each of which will be discussed in this text.

The active regions of III-nitride based LEDs are composed of $In_xGa_{1-x}N$, the bandgap of which can be tuned to attain the desired wavelength depending on the percent composition of indium. An issue with this design is that the optimal growth temperature of InGaN is lower than that of GaN, making the growth temperature of the top p-layers critical to the device performance. Thus, an InGaN:Mg layer was used as the hole injection and p-contact layers for a green led, which can be grown at a lower temperature than GaN:Mg in order to maintain the integrity of the active region. However, the use of InGaN comes with its own set of drawbacks, specifically the formation of V-defects. Several methods were investigated to suppress these defects such as graded p-layers, short period superlattices, and native GaN substrates. As a result, LEDs emitting at ~532 nm were realized.

The epitaxial structure for a III-nitride LD is more complicated than that of an LED, and so it faces many of the same technical challenges and then some. Strain

engineering and defect reduction were the primary focuses of optimization in this study. Superlattice-based cladding layers, native GaN substrates, InGaN waveguides, and doping optimization were all utilized to lower the probability of defect formation. This thesis reports on the realization of a 454 nm LD, with higher wavelength devices to follow the same developmental path.

CHAPTER 1

INTRODUCTION

Semiconductor based monochromatic light sources have long been used for such things as power indicators and laser pointers. But recent developments have pushed the technology from niche applications to general use in solid state lighting and full color displays. Visible red light emitters, including light emitting diodes (LEDs) and laser diodes (LDs) based on GaAsP, were invented by Holonyak et al. in 1962 [3]. Modern incarnations of red LEDs consist of InAlGaP and AlGaAs. Commercially viable blue LEDs, based on InGaN, were pioneered by Nakamura et al. in 1994 [4] with the blue LD following in 1996 [5]. The missing link for full color displays and white light is thus a green light emitter. Figure 1 shows the external quantum efficiency of the best reported LEDs at various emission wavelenghts. As one approaches "true green" or ~530 nm from either side of the visible spectrum, the efficiency drops off for both the (Ga,In)N and (Al,Ga,In)P material systems. This is known as the "green gap." This thesis will discuss efforts to overcome the technical challenges and improve the efficiency of III-nitride based green LEDs and LDs for the commercialization of red-green-blue full spectrum light emitters.

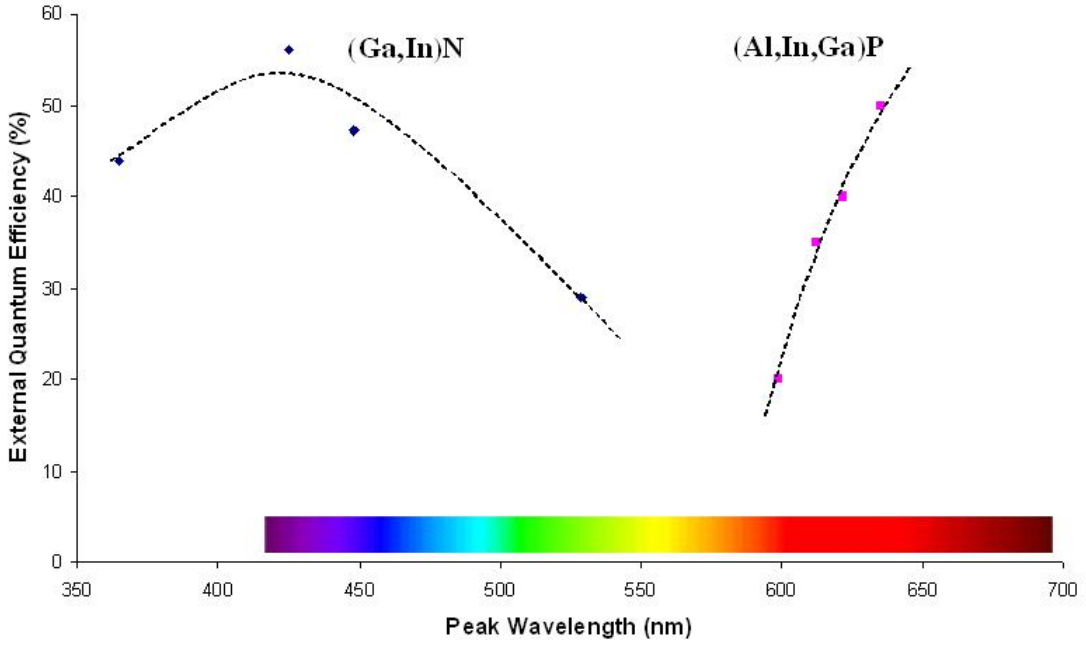

Figure 1.1: External quantum efficiency of state of the art LEDs under high power at room temperature. Adapted from Krames, et al. [1].

1.1 III-Nitride Materials

III-nitrides have seen wide use in high power electronic applications due to their wide bandgap and high thermal stability. They also have a direct bandgap, which makes them ideal for optoelectronic applications, as opposed to silicon which has an indirect bandgap. The binary combinations of III-nitrides cover a wide range of the electromagnetic spectrum in bandgap energy (Figure 1.2), from AlN in the ultraviolet (6.2 eV, 200 nm), to InN in the infrared (0.7 eV, 1772 nm), and GaN in between (3.4 eV, 364 nm). The ternary combinations, such as InGaN and AlGaN, fill in the gaps based on composition as per Vegard's law:

$$E_{g,In_xGa_{1-x}N}(x) = x \cdot E_{g,InN} + (1-x) \cdot E_{g,GaN} + bx(1-x) \tag{1.1}$$

$$a_{In_xGa_{1-x}N}(x) = x \cdot a_{InN} + (1-x) \cdot a_{GaN} + bx(1-x) \tag{1.2}$$

where E_g is the bandgap energy, a is the lattice parameter, x is the % alloy composition (in $In_xGa_{1-x}N$ or $Al_xGa_{1-x}N$), and b is the bandgap bowing parameter specific to each compound and determined experimentally.

The nitrides have a hexagonal/wurtzite crystal lattice and thus four axes: the c-axis perpendicular to the basal planes, and three a-axes perpendicular to the c-axis as shown in Figure 1.3. The Bravais lattice of both the hexagonal and trigonal crystal systems are unique in that they have 120° rotational symmetry, with hexagonal having an addition six-fold symmetry about the c-axis. So while the Miller indicies of the hexagonal system can be expressed with just three vectors – a_1, a_2, and c or (hkl) – an additional vector 120° from a_1 and a_2 is often used to yield the four-axis Miller-Bravais indices in the form ($hkil$). Since the intercept of the plane on this a_3 axis is determined by its intercept on a_1 and a_2, the Miller-Bravais indices share the relationship: $i = -(h+k)$.

In the cubic crystal system, crystal directions given by [XYZ] are numerically equivalent to the Miller indices of the perpendicular plane, i.e. [XYZ] = [hkl]. But this is not necessarily the case for all directions in every other crystal system. This complicates the directional scheme in the hexagonal crystal system, and the conversion from three- to four-index directions is not straightforward.

Directions in a hexagonal lattice can be described by three coordinates: [XYZ], corresponding to vectors parallel to a_1, a_2, and c. To recognize the inclusion of the a_3 axis, a fourth coordinate is added yielding a new set of directional vectors, [$uvtw$], such that $u = X + t$, $v = Y + t$, $t = -(u + v)$ and $w = Z$. Note that the sum of the three new basal plane vectors is equal to zero yielding $t = -(X+Y)/3$. Therefore, converting from three- to four-coordinate directions is accomplished by the following equations:

$$u = X - \frac{(X+Y)}{3} = \frac{2X - Y}{3} \tag{1.3}$$

$$v = Y - \frac{(X+Z)}{3} = \frac{2Y - X}{3} \tag{1.4}$$

$$t = -\frac{(X+Y)}{3} \tag{1.5}$$

$$w = Z \tag{1.6}$$

A critical challenge of nitride growth is in the selection of a lattice-matched substrate. C-plane sapphire (Al_2O_3) is commonly used due to its hexagonal symmetry, thermal stability, availability, and low cost. However there is ~14% lattice mismatch between GaN and the Al bonding sites on sapphire which results in crystal strain and defect formation in epitaxially grown layers.

Single-crystal GaN was first grown and characterized in 1969 by Maruska and Tietjen by hydride vapor phase epitaxy (HVPE) [6]. The first instance of GaN growth using metalorganic chemical vapor deposition (MOCVD), now the preferred method, was by Manasevit, et al. in 1971 [7]. The early work in GaN epitaxy was plagued by the lack of lattice matched substrates which resulted in poor crystal quality, and high defect density in the range of 10^{11} cm^{-2}. Furthermore, these films all had a high background carrier density of 10^{19} cm^{-3} which made it difficult to control n-type doping, and nearly impossible to create p-type conduction. This hindered interest in commercial development of III-nitrides as the p-n junction is a staple of semiconductor devices.

A major breakthrough occurred in 1985 when Amano and Akasaki grew the first high-quality GaN epitaxial films on sapphire using a low-temperature AlN buffer layer by MOCVD [8]. The dislocation density was reduced to ~10^9 cm^{-2} and the intrinsic background electron concentration was lowered to 10^{16} cm^{-3}. The low-temperature (LT) buffer layer allows for the nucleation of 3D islands which lowers the interfacial free energy between the substrate and thin film. The following high-temperature layers grow laterally across the dense island cluster, resulting in a high-quality and uniform film.

Due to the reduced background carrier concentration, n-type doping of GaN layers could now be controlled. Doping in gallium nitride is achieved by atomic substitution of either Ga or N by a dopant atom. Donor (n-type) dopants for GaN include group IV elements, notably germanium and silicon. These act as donors since they favor replacement of the Ga atom over N due to the lower difference in covalent radii as can be seen in Table 1. Doping efficiency is quite high for silane (SiH_4), with reported carrier concentrations as high as $n = 2 \times 10^{19}$ cm^{-3} via MOCVD [9]. Silane doping was also found to maintain crystal quality, even at high doping concentrations.

P-type doping requires a bit more effort. Magnesium is a commonly used acceptor which replaces the Ga atom as is the case with silicon. However it is compensated by hydrogen within the GaN crystal [10]. In order to activate the Mg acceptor, this hydrogen bond must be broken by some method such as low energy electron beam irradiation (LEEBI) [11], or thermal annealing [12]. But even then, the doping efficiency is quite low at ~1%, meaning that a magnesium concentration as high as 10^{20} cm^{-3} will yield a carrier concentration of only 1×10^{18} cm^{-3}. The covalent radius of Mg is also larger than that of Ga, which leads to degradation of crystal quality at high concentrations.

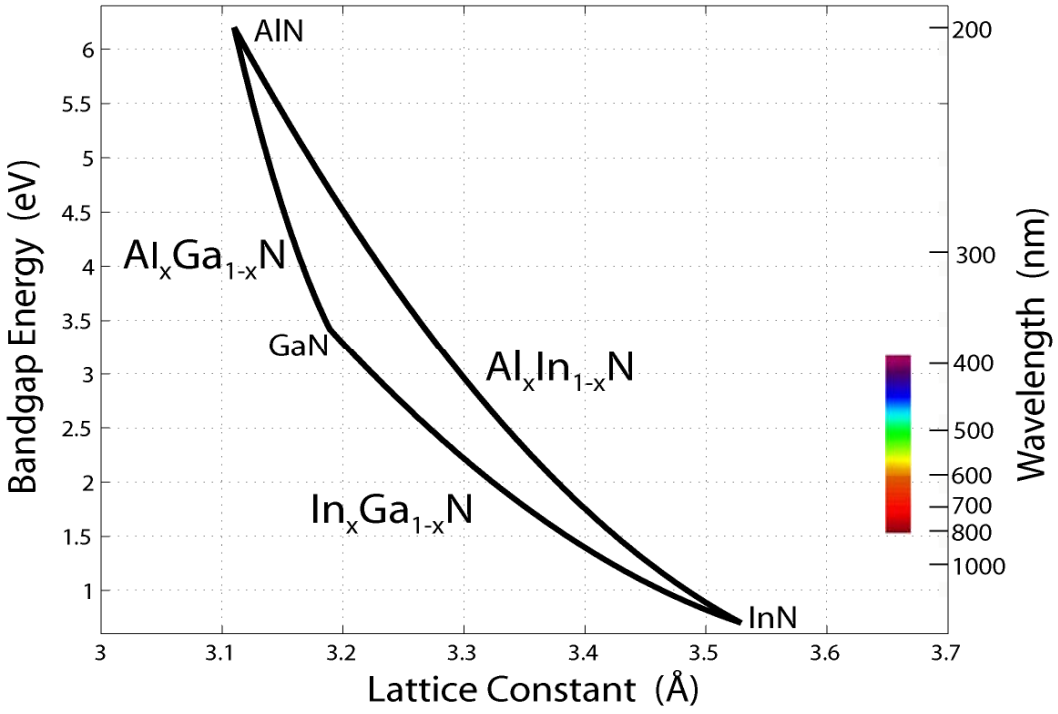

Figure 1.2: Bandgap energy vs. lattice constant for III-nitride materials.

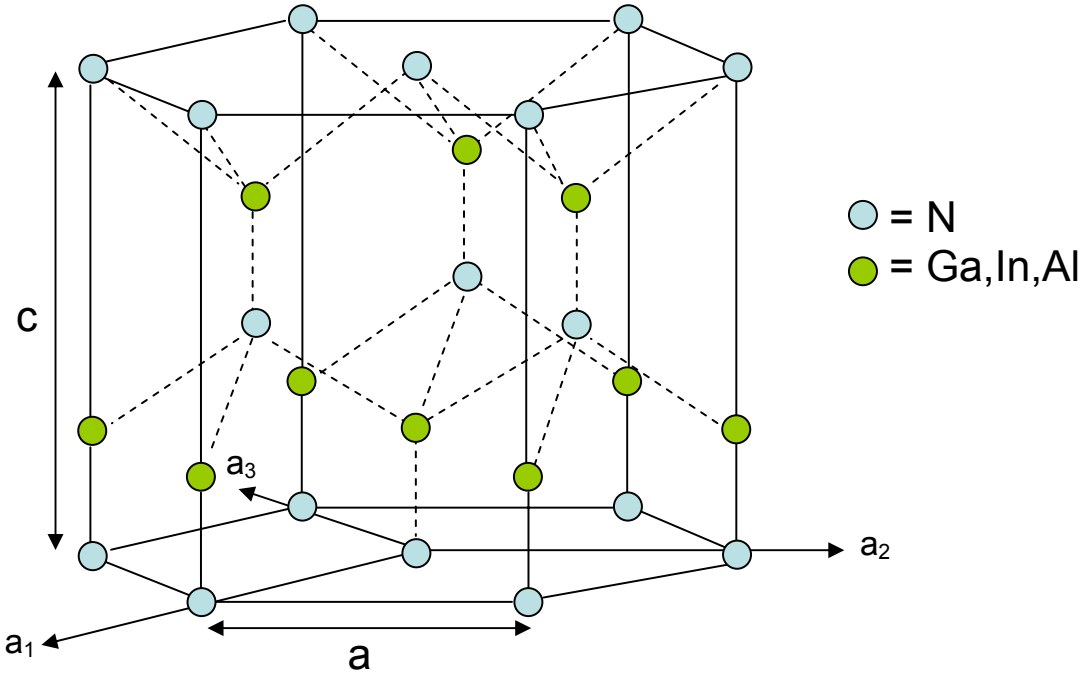

Figure 1.3: Hexagonal wurtzite unit cell of III-nitride crystal.

Table 1.1: Covalent radii of gallium, nitrogen and common GaN dopants.

Atom	Covalent Radius (Å)
Gallium	1.26
Nitrogen	0.75
Silicon	1.11
Germanium	1.22
Magnesium	1.36
Indium	1.44
Aluminum	1.18

1.2 Metalorganic Chemical Vapor Deposition

The process of metalorganic chemical vapor deposition (MOCVD) was pioneered by Manasevit in 1968 [13]. In the years that followed, he was successful in demonstrating the deposition of several various materials onto semiconductors and insulators, such as GaAs, GaP, GaAlAs, AlN and GaN [7]. However, these epitaxial layers often suffered from impurity related defects, as the metalorganic sources and reactor designs were still in their infancy. The first practical devices grown using MOCVD were the AlGaAs/GaAs solar cells and quantum well injection laser by Dupuis, et al. in 1977 and 78 [14, 15]. This set off a flurry of research in the area which has led to large-scale commercialization of MOCVD grown devices such as LEDs and high electron mobility transistors (HEMTs).

The primary use of MOCVD is for the growth of III-V epitaxial layers. It is favored by industry because it is well developed, scalable, and functions at pressures close to atmospheric. As the name implies, metalorganic compounds are used as the precursors. These usually consist of an organic trimethyl or triethyl group connected to a group III metal such as Ga, Al, or In. Group V precursors come in the form of hydrides such as AsH_3 (arsine) or NH_3 (ammonia).

As discussed previously, good n-type doping can be accomplished with silicon using SiH_4 as a precursor. The issues surrounding p-type doping using magnesium with

bis(cyclopentadienyl)magnesium (Cp_2Mg) as a precursor are further complicated by the "memory effect" [16]. Mg source molecules have a large sticking coefficient and thus are prone to sticking to the walls of the reactor before reaching the substrate. This results in reduced Mg incorporation into the sample, or a gradual "turn on" as Mg first adsorbs to the walls and then to the surface [16]. To avoid this, a pre-growth Mg coat is used to saturate the Mg coating on the reactor walls.

An inert carrier gas, H_2 or N_2, is used to carry the precursors to the reaction chamber. The precursors are broken by pyrolysis and adsorb onto the substrate. Epitaxial crystals are formed by the chemical reaction:

$$A_3M\ (g) + EH_3\ (g) \rightarrow ME\ (s) + 3AH\ (g) \tag{1.7}$$

where A is the alkyl group of CH_3 or C_2H_5, M is the group III metal, E is the group V atom, and H is hydrogen.

Nitride work using MOCVD moved rapidly in the late 1980s, with the major breakthrough of two step growth by Amano, et al. in 1986 [8]. The same group was successful in p-doping gallium nitride in 1989 [11]. In 1992, Nakamura provided the final breakthroughs in the high-quality growth of InGaN on GaN needed for blue and green double heterostructure optoelectronic devices via his two-flow reactor design [17]. Commercialization of the InGaN blue LED and LD soon followed.

The MOCVD reactor used for this thesis is a Thomas Swan 6x2" rotating disk reactor with a close coupled showerhead (CCS). The CCS enables for the intermixing of precursors within close proximity to the substrates, resulting in uniform deposition. A three zone heater allows for control of temperature gradients within the chamber, to further control uniformity.

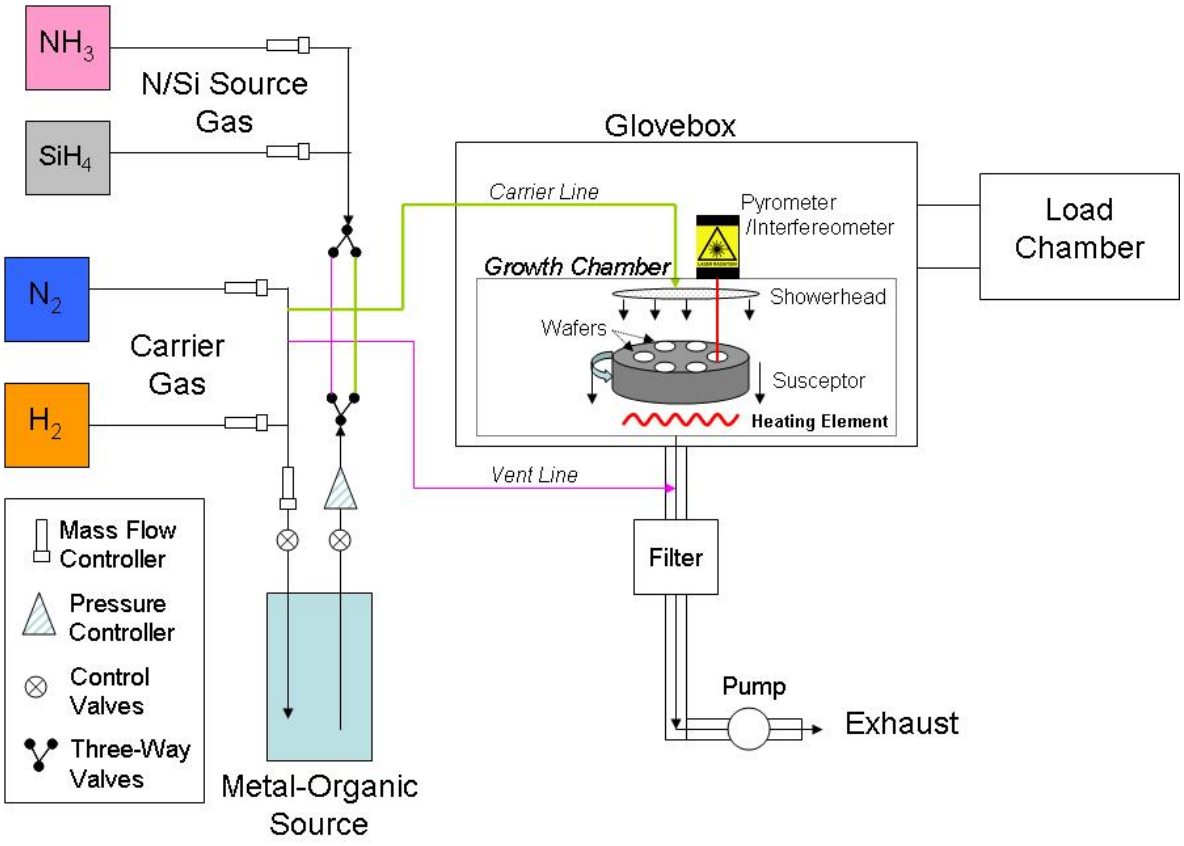

Figure 1.4: Basic diagram of an MOCVD reactor. Not to scale.

CHAPTER 2

MATERIAL CHARACTERIZATION TECHNIQUES

Several methods are employed to measure the properties and quality of MOCVD grown epitaxial layers. Since there is often a direct correlation between material quality and device performance, these methods are useful metrics to predict fabricated device results. Described here are atomic force microscopy, photoluminescence, electroluminescence, scanning electron microscopy, secondary ion mass spectrometry, Hall-effect measurement, and x-ray diffraction.

2.1 Atomic Force Microscopy

The atomic force microscope (AFM) was first developed in 1986 by Binnig, Quate, and Gerber [2]. It consists of five major components: a cantilever, probe tip, sample stage, measurement device, and feedback mechanism. The probe tip is the needle which senses the sample, and must be as sharp as possible to achieve sub nanometer scale resolution. An ideal tip has a diameter of just one atom at its apex. The probe is attached to the cantilever which acts as a spring, the spring constant of which must be extremely small in order to detect forces in the range of $10^{-8} - 10^{-12}$ N (with a theoretical lower limit of 10^{-18} N) and deflections as small as 10^{-4} Å according to Hooke's law:

$$F = -kx \tag{2.1}$$

where F is the force applied, k is the spring constant, and x is the displacement of the spring.

In the original design of the AFM (Figure 2.1a), a scanning tunneling microscope (STM) was used to measure the deflection of the cantilever. Figure 2.1b depicts a modern incarnation of the AFM in which the STM has been replaced with a laser and photodiode, known collectively as the "scanner."

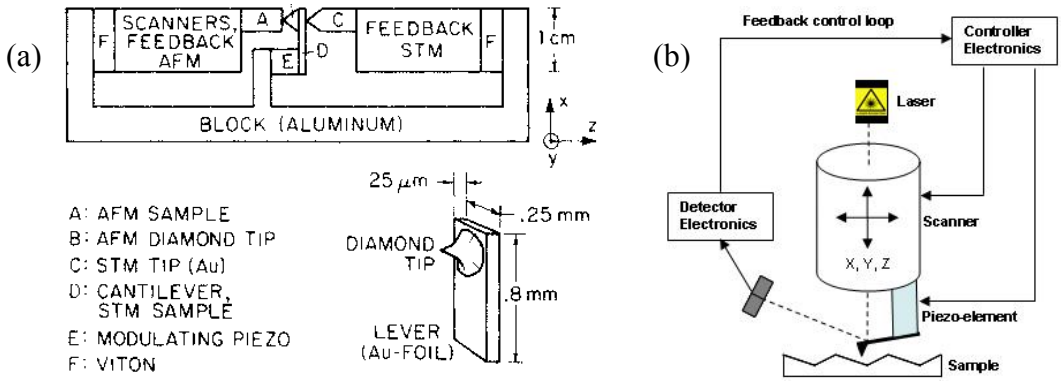

Figure 2.1: Anatomy of an AFM. (a) The original device invented by Binnig, et al. in 1986 [2]. (b) Modern incarnation of an AFM.

Atomic force microscopy has three primary modes of operation: contact, tapping, and non-contact. In contact mode, the probe tip is kept in physical contact with the sample at all times as it is raster scanned across the surface. The cantilever deflection is measured by the laser and photodiode and used to construct the image by the detector electronics. The feedback mechanism ensures a constant force between the probe tip and sample surface by a piezoelectric element in the scanner.

In tapping mode, the cantilever is oscillated at its resonant frequency by a piezoelectric element in the scanner, close to the cantilever. The probe tip then taps the sample surface at that frequency. As the cantilever oscillates, the reflected laser also

oscillates over the photodiode. The computer measures the amplitude, frequency, and phase of this oscillation to create an image, and also provide feedback to the scanner piezoelectric which will adjust the height of the probe to ensure a constant oscillation frequency.

In non-contact mode, the probe tip is oscillated at or slightly above its resonant frequency. The tip is scanned just above the surface, close enough to be deflected by interatomic force interactions such as Van der Walls forces. These forces dampen the oscillation, which is detected by the laser and photodiode measurement.

The AFM used in this thesis is a Veeco Dimension 3100 scanning probe microscope operated in tapping mode. High resolution scans are obtained at 5 x 5 μm^2.

2.2 Photoluminescence

Photoluminescence (PL) is an optical characterization technique primarily for determining the band gap energy of a material, but can also be used to determine material quality. The basic premise is based on radiative recombination. If energy is added to a semiconductor in excess of the forbidden energy bandgap, an electron will be excited from the valence band to the conduction band, leaving behind a "hole" which is an imaginary particle, but convenient way to model the lack of an electron. If the energy is very high, electrons can be excited to an energy state above the conduction band, but with no energy barrier in the way, most will naturally fall to the conduction band edge, emitting heat or transferring energy to secondary/Auger electrons. In PL, this excitation energy is in the form of a light source, typically a high energy/short wavelength laser.

For direct bandgap semiconductors, the majority of the electron-hole pairs will recombine at the band edge energy, emitting photons of the corresponding wavelength as per the relation:

$$E_g = hv = h\frac{c}{\lambda} \tag{2.2}$$

where E_g is the bandgap, h is Plank's constant, v is frequency of light, c is speed of light, and λ is the wavelength.

A detector composed of a monochromator and CCD scans the spectrum and records the intensity at each wavelength. The peaks in intensity correspond to the bandgap energy of the material. Since the material is not perfect, each peak will be broadened and thus have a measurable line width. Sub-bandgap levels created by dopants and defects will broaden the spectrum or produce peaks of their own.

PL measurements in this thesis were performed using an Accent RPM 2000 with 2 mW 266 nm Q-switched laser as the excitation source. PL measured in this way is not a specific metric of luminous intensity or light output. Rather, it is used to compare the brightness between samples. Therefore, the light intensity in a PL measurement is given in terms of arbitrary units (a.u.). Data from multiple samples are usually plotted together to determine which is brighter.

2.3 Electroluminescence

Electroluminescence (EL) is a test of the electrical and optical properties of a material and/or device. Unlike photoluminescence, which optically excites the material to create electron-hole pairs, EL injects carriers into the material through electrical contacts. The injected carriers will recombine throughout the material, emitting photons at the bandgap energy. Quantum wells increase the probability of recombination, and so the major peak will be at the energy bandgap of these wells. Emission at other wavelengths can indicate an overflowing of the wells, or recombination at some other site in the material. Defects create non-radiative recombination centers and will thus degrade the EL performance of the device. As with PL, the measured intensity from EL is given in terms of arbitrary units. Current-voltage curves can also be simultaneously measured using EL by plotting the applied current versus voltage, which gives some idea of the electrical performance of the device.

2.4 Hall-Effect Measurement

The Hall-effect measurement, as put to practice by LJ Van der Pauw in 1958 [18], is a simple way to measure the resistivity, majority carrier type, majority carrier concentration, and carrier mobility of a semiconductor sample. An approximately 1 x 1 cm^2 square sample is prepared by depositing an ohmic contact to each corner. The contact is ideally infinitely small, but pragmatically smaller than the distance between contacts. Indium eutectic is commonly used for contact to n-type III-nitride material, and evaporated Ni/Ag/Pt for p-type III-N contact.

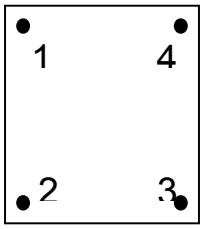

Figure 2.2: A typical hall sample; variation on Van der Pauw Geometry.

Free-standing resistivity is measured by applying a current across one pair of contacts and measuring the voltage across the other pair in the two configurations as per the following equation:

$$\rho = 2.266t\left(\frac{V_{43}}{I_{12}} + \frac{V_{23}}{I_{14}}\right)F \tag{2.3}$$

where t is the sample thickness, I is the applied current, V is the measured voltage, and F is a correction factor based on sample symmetry (1 for a perfect square).

Carrier concentration and mobility are derived from the Hall coefficient. When a magnetic field is applied perpendicular to an applied current, the resulting Lorentz force pushes the carriers to one side, creating an electric field normal to the current. The voltage produced by this electric field yields the Hall coefficient by,

$$R_H = \frac{V_h \cdot t}{I \cdot B} \tag{2.4}$$

where V_h is the Hall voltage, t is the sample thickness, I is the applied current, and B is the applied magnetic field. The polarity of V_h is determined by the material: positive for p-type and negative for n-type. The free-carrier concentration and mobility follow thusly:

$$N = \frac{1}{qR_H} \tag{2.5}$$

$$\mu = \frac{R_H}{\rho} \tag{2.6}$$

The Hall measurements carried out for this thesis were performed using an Accent HL5500PC Hall measurement system.

2.5 Secondary Ion Mass Spectrometry

Secondary ion mass spectrometry (SIMS) is a powerful method that produces a 2D profile of a sample in the form of molecular concentration as a function of depth. Layer thickness, doping concentration, background contamination concentrations and interface quality can thus all be observed empirically. The drawback is that this is a destructive process.

In SIMS, the sample is sputtered by a primary ion beam composed of an ionized species such as O_2^+ or Cs^+. Atomic and molecular secondary ions are thus released from the sample surface. A mass analyzer scans the spectrum of mass to charge ratios and counts the ions at each step (in ions per second). Since every element has a roughly unique mass to charge ratio, the peaks of the ion counts correlate to the elements under investigation. As the sample is sputtered, the ion count is plotted over time for each

element. At the end of the sputtering, the depth of the sputtered crater is measured using a profilometer. That depth divided by time yields average sputter rate from which an elemental depth profile can be calculated. The ion count is converted to elemental concentration (atoms/cc) via the following equation:

$$C_E = RSF \cdot \frac{I_E C_M}{I_M} \tag{2.7}$$

where C_E is the concentration of the element of interest, RSF is its relative sensitivity factor, I_E is the secondary ion intensity for the element of interest, C_M is the major/matrix element concentration, and I_M is the ion intensity of the major element. The concentration versus depth profile is thus obtained.

2.6 Scanning Electron Microscopy

Scanning electron microscopy (SEM) is a powerful tool in micro- and nano-electronics allowing surface resolution to the nanometer scale, and exceeding 100,000x magnification. The basic premise revolves around inelastic electron scattering.

In SEM, an electron gun produces a beam via thermionic emission from a tungsten filament. These electrons have energy on the scale of several keV. The beam is focused and accelerated by a magnetic coil. When the narrow beam is incident upon the sample surface, the high energy primary electrons excite the sample, and are able to cause the discharge of secondary electrons. As the primary beam is raster scanned over the sample surface, secondary electrons with different energies and trajectories are released. These secondary electrons are gathered by a detector and processed via computer into an

image of the surface. The detector is able to filter out the secondary electrons from stray primary electrons, and any electromagnetic radiation that results from electron bombardment of the surface. Thus a very good picture of the surface morphology of a sample can be obtained.

One drawback of the SEM is that it must be performed under high vacuum to prevent atmospheric scattering of the electron beam. It also has difficulty measuring insulating samples for extended periods of time. Note that the measuring mechanism is by definition electrically charged. A conducting sample is able to evenly distribute this charge while an insulating sample will yield a charge buildup in the scan area over time. This built-up charge can deflect the primary beam, causing a shift in the image. Therefore, SEM for III-nitride samples is best done in a short amount of time and over larger areas (micron scale) to prevent any large buildup of electrons in a small area.

2.7 X-ray Diffraction

X-ray diffraction (XRD) is a useful method to determine the lattice constant, alloy composition, strain, and superlattice period of a crystal structure.

The x-ray data used in this report was obtained with a Phillips X'Pert MRD High Resolution X-ray diffractometer. The x-ray source emits characteristic Cu K_α radiation that is collimated by a four crystal Ge (220) Bartels monochromator, which enables 0.00001° resolution.

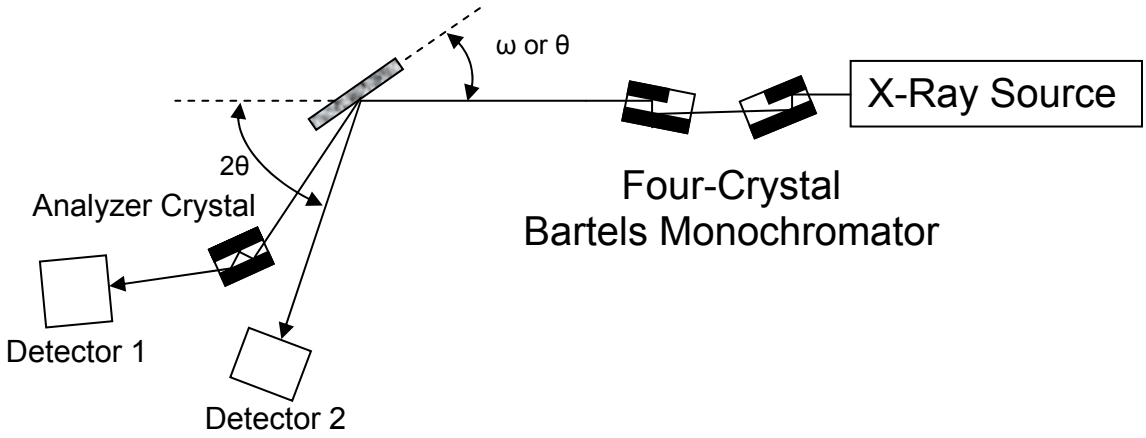

Figure 2.3: Schematic diagram of an X-ray diffraction setup.

The basic principle of XRD is based on Bragg's law:

$$n\lambda = 2d_{hkl}\sin\theta_B \tag{2.8}$$

where n is an integer representing the diffraction order, λ is the incident wavelength, d_{hkl} is the spacing of the crystal planes, and θ_B is the Bragg angle. For a cubic crystal, the lattice spacing of the plane (*hkl*) is given by:

$$\frac{1}{d_{hkl}^2} = \frac{h^2 + k^2 + l^2}{a^2} \tag{2.9}$$

For a hexagonal Bravais lattice, the lattice spacing is given as:

$$\frac{1}{d_{hkl}^2} = \frac{4}{3}\left(\frac{h^2 + hk + k^2}{a^2}\right) + \frac{l^2}{c^2} \tag{2.10}$$

where d_{hkl} is the spacing between planes, a and c are lattice constants, and h, k, and l are the Miller indices of the plane of interest. When the x-ray is incident upon the sample at the Bragg angle for a given set of crystal planes (or "Bragg planes"), the reflections from those planes constructively interfere, creating an intensity spike at the detector. Bragg planes of the form (*00l*) are called symmetric planes, while all others are known as asymmetric planes. The c lattice constant can be determined from a single symmetric XRD scan by combining equations 2.8 and 2.10 to get

$$c = \frac{n\lambda l}{2\sin\theta} \tag{2.11}$$

The most commonly used XRD scan is the rocking curve otherwise known as the ω-scan. In this configuration, the detector is kept at a fixed angle relative to the primary beam (2θ) while the sample is rotated or "rocked" across the ω axis, perpendicular to the schematic diagram in Figure 2.3. Rocking curves are useful for determining the c lattice constant via equation 2.11. In a perfect crystal with no strain or defects, the ω-scan produces a δ-function at the Bragg angle. But in the presence of imperfect plane spacing, the Bragg peak is broadened. The full width half maximum (FWHM) or linewidth of this broadened peak is useful for comparing the relative quality of different samples. Asymmetric rocking curves on planes such as $(10\bar{1}2)$ or $(10\bar{1}4)$ can provide more information since the FWHM of these Bragg peaks are sensitive to threading dislocations [19, 20].

One drawback of the rocking curve is that since the detector is not moved along with the sample, they have a limited angular range of only ~1º. For III-nitride materials grown on non-native substrates with large lattice mismatch (e.g. sapphire), the Bragg angles for the epitaxial layers are much smaller than that of the substrate such that film/substrate lattice mismatch information cannot be gathered in a single scan.

The ω-2θ scan can overcome this limitation. In this configuration, the detector moves at twice the angular rotation rate as the sample so that the measured diffraction angle is always 2θ with respect to the transmitted incident beam. Therefore, scans over larger angles can be taken and data can be gathered for multiple layers. Furthermore, the diffractions peaks are narrower, reducing the overlap between layers in the diffraction spectrum, allowing for better analysis of individual layers.

Reciprocal space mapping (RSM) is a powerful technique made possible by XRD. In this configuration, an ω-2θ scan is plotted against a rocking curve in reciprocal space. The resulting two-dimensional image allows for the analysis of strain and relaxation between layers, in addition to the relative crystal quality of each layer. In an asymmetric RSM, both the *a* and *c* lattice constants can be directly calculated from the reciprocal lattice vectors corresponding to the peak positions. The FWHM of each peak along the ω directional corresponds to the "mosaicity" of the associated layer: if it has many disoriented grain boundaries the FWHM will be large, while a more ideal single crystal will have a lower FWHM. The FWHM along ω-2θ indicates the level of fluctuations in the *c*-lattice constant, which result from uneven strain in the material or compositional grading. If the centers of each peak are vertically aligned along the same ω (i.e. they share a common Bragg angle and thus common plane spacing and common lattice

constants) then the layers are fully strained. Displacement of peaks in the horizontal direction indicates that relaxation has taken place. While a basic description has been given here, a more detailed look at RSM and its geometric significance can be found elsewhere [21, 22].

CHAPTER 3

DEVICE BASICS

This chapter will review the operation of light emitting diodes and laser diodes. Basic device structures and technical challenges will be discussed.

3.1 Light Emitting Diodes

3.1.1 Electrical Injection and Radiative Recombination

The LED is a p-n junction device that functions under forward bias. Charge carriers are injected via electrical contact: holes at the p-type contact, electrons at the n-type side. The carriers recombine across the junction, and under the right conditions will emit a photon (Figure 3.1). This is called radiative recombination.

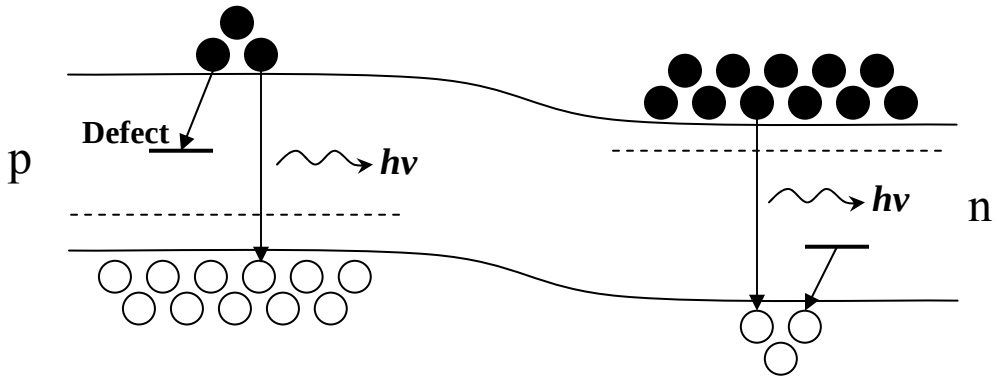

Figure 3.1: Energy band diagram of a p-n junction under forward bias featuring radiataive recombination.

The wavelength of this light is determined the energy bandgap of the semiconductor as per Equation 2.2. The active region of visible III-nitride LEDs is typically $In_xGa_{1-x}N$, the bandgap of which is tuned by varying x, which in turn tunes the wavelength of emission.

Defects in the material and sub-bandgap energy states can result in non-radiative recombination of carriers, the product of which is a phonon or heat. Radiative and non-radiative recombination are quantized by a parameter known as recombination lifetime by the following relationship:

$$\frac{1}{\tau} = \frac{1}{\tau_r} + \frac{1}{\tau_{nr}} \tag{3.1}$$

where τ_r and τ_{nr} are the radiative and non radiative lifetimes respectively. The probability of radiative recombination occurring is calculated as the internal quantum efficiency (IQE) by

$$\eta_{IQE} = \frac{1/\tau_r}{1/\tau} \tag{3.2}$$

In an ideal case, τ_{nr} is 0 making the IQE equal to 1. But for practical applications, the technical challenges lie in reducing non-radiative recombination as much as possible by limiting the formation of defects.

3.1.2 Double Heterostructures and Quantum Wells

The IQE can be improved if the charge carriers are physically confined, increasing the probability of radiative recombination. One way to accomplish this is with a double heterostructure, where a narrow bandgap material is sandwiched between two

materials of larger bandgap, for example InGaN between GaN as shown in Figure 3.2. Charge carriers always "prefer" lower energy states, and so charge diffusion will concentrate the carriers within the central region. Thus there are more electron-hole pairs readily available for radiative recombination.

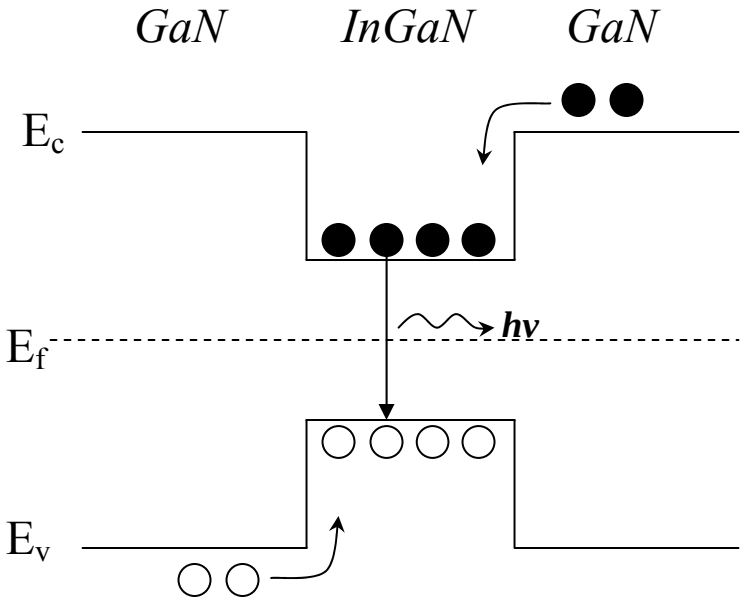

Figure 3.2: Energy band diagram of a GaN/InGaN/GaN quantum well with electrical carrier injection and radiative recombination.

If the central region of this structure is narrow enough, it effectively limits the carrier movement to two dimensions, and is known as a quantum well. In InGaN LEDs, the well width is typically in the range of 3 nm. This enhanced confinement leads to enhanced IQE. Since there are a finite number of energy states per well, multiple quantum wells (MQW) can be used to prevent well filling, thus increasing the amount of band-to-band radiative recombination.

3.1.3 Technical Challenges

Quantum wells are the structure of choice for commercial LEDs. However, they still involve several technical challenges to be overcome, especially as the wavelength approaches 500 nm and above.

Quantum-Confined Stark Effect

Since GaN is a polar structure (when grown in the c-axis direction), is contains a spontaneous electric polarization field. Even with no external bias applied, this internal bias will exert influence on carrier motion. Furthermore, built-in strain between hetero-epitaxial layers produces piezoelectric fields, resulting in large internal biases. In quantum wells, this piezoelectric field separates charge carriers, inhibiting the radiative recombination of electron hole pairs. This is known as the quantum-confined Stark effect (QCSE), and is particularly important in InGaN quantum wells, where the strength of the internal fields can be as high as 1-2 MV/cm [23].

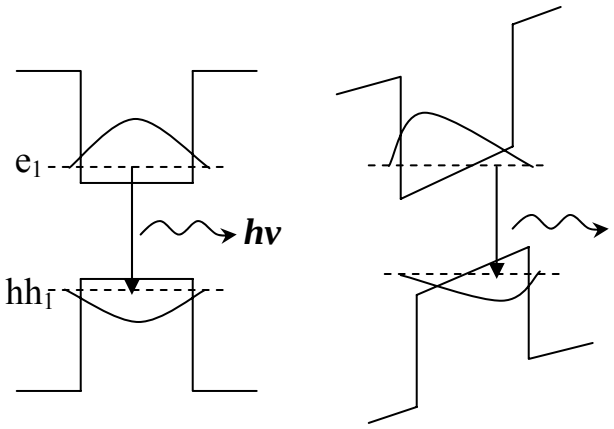

Figure 3.3: Band diagrams demonstrating the quantum-confined Stark effect. A quantum well with (a) no electric field and another (b) in the presence of an electric field.

QCSE-induced band bending also allows carriers to recombine at levels below the bandgap of the material, resulting in a red-shift in the emitted wavelength, particularly at low injection levels. At higher injection levels, the QCSE is screened as more carriers are pumped into the wells, reducing charge separation and creating more instances of electron-hole overlap which favors radiative recombination.

InGaN Decomposition and Segregation

Green light emitters require high indium composition in $In_xGa_{1-x}N$ in the range of x = 30%. This creates a challenge in epitaxial growth as InGaN requires a lower temperature than GaN (around 740 ºC for green InGaN wells as opposed to 1000+ ºC for GaN), complicating InGaN/GaN MQW growth, and also requiring a reduced growth temperature for the p-type contact layer so that indium does not desorb. Lowering the growth temperature of the InGaN regions will increase the indium content, but reduce the quality of following layers since they are usually optimized at higher temperatures, resulting in a trade-off between active region and contact layer quality. The selection of carrier gas is also restricted to nitrogen, as hydrogen has the effect of "stripping" indium from InGaN layers [24, 25].

Furthermore, indium has a tendency to form non-uniform alloys for InGaN materials. Dislocations tend to favor indium clustering [26] and temperature gradients across the substrate can lead to segregation of indium. Since higher indium content means lower bandgap, a non-uniform distribution of energy potentials will form across quantum well layers and photons of different energy (and thus different wavelength) will be

emitted from different parts of the wafer. This can be observed in the emission spectrum of an LED via a broadening of the linewidth from the central peak wavelength.

Efficiency Droop

As interest in InGaN LEDs for solid state lighting applications has grown in recent years, the input power for these devices has increased in an effort to increase the luminous intensity. However, a bizarre effect takes place at these high input powers where the efficiency of the device drops off or "droops" to levels below that of fluorescent bulbs. For LEDs to be competitive in general illumination applications, this effect must be mitigated. But first it needs to be explained.

There have been several possible explanations for efficiency droop including Auger recombination [27], electron overflow [28], lack of hole injection [29], internal heating effects [30], and defects [31]. The debate as to the cause and solution of efficiency droop are still ongoing and the focus intense research.

3.2 Laser Diodes

3.2.1 Stimulated vs. Spontaneous Emission

When an electron-hole pair undergoes band-to-band recombination emitting a photon as described in the previous section, it is known as "spontaneous recombination" due to the random nature of the process, and the resulting photons are emitted in a variety of directions. This is the fundamental operational mode of an LED.

Laser diodes work a bit differently. When a photon with energy $E_{ph} > E_g$ is incident upon a semiconductor, two things can happen: the photon can be absorbed by the

material, exciting an electron from the valence to the conduction band, or it can stimulate the radiative recombination of an electron-hole pair, otherwise known as stimulated emission. If this second photon has the same frequency and direction as the first, the two photons create coherent light.

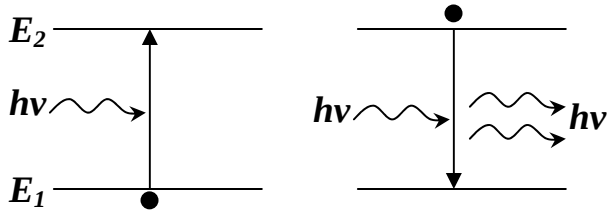

Figure 3.4: Energy band diagrams featuring (a) photonic absorption and (b) stimulated emission.

Population inversion occurs when the minority carriers in a p-n junction outnumber the majority carriers. This is accomplished either by optical excitation, where the diode is pumped by another laser, or by electrical injection at very high current densities. A diode is said to be "lasing" when population inversion leads to the stimulated emission of coherent light.

Before quantum theory was fully developed, Einstein mathematically described the transition probabilities of absorption, spontaneous emission, and stimulated emission. He considered two energy states, E_1 and E_2, analogous to the valence and conduction bands in a semiconductor ($E_1 \sim E_v$, $E_2 \sim E_c$), with $E_2 > E_1$ and $E_2 - E_1 = hv$. Each level has a respective electron density, N_1 and N_2, which are related by equation 3.3 in equilibrium:

$$\frac{N_2}{N_1} = \exp(-hv / k_B T) \tag{3.3}$$

where k_B is the Boltzmann constant and T is temperature. In an unperturbed state, $N_1 > N_2$. The probability of a transition from E_1 to E_2 (i.e. absorption) is given by

$$W_{12} = N_1 \varphi(v) B_{12} \tag{3.4}$$

where B_{12} is known as the Einstein absorption coefficient and $\varphi(v)$ is the radiation density of photons with frequency v, defined as $\varphi(v) = N_{ph} hv$ where N_{ph} is the number of photons present. A transition from E_2 to E_1 can occur as spontaneous or stimulated emission, the probability of which is

$$W_{21} = N_2 A_{21} + N_2 \varphi(v) B_{21} \tag{3.5}$$

where A_{21} and B_{21} are the Einstein coefficients for spontaneous and stimulated emission respectively, further defined by $A_{21} = 1/\tau_r$ and $B_{21} = \lambda^3/8\pi\tau_r$ [32]. Under thermal equilibrium, the probabilities of upward and downward transition are equal or

$$N_1 \varphi(v) B_{12} = N_2 A_{21} + N_2 \varphi(v) B_{21} \tag{3.6}$$

The Einstein relations also state that $B_{12} = B_{21}$ under equilibrium.

As with an LED, the rate of emission must exceed that of absorption and non-radiative recombination for a laser diode in order to break the equilibrium condition and produce light. Thus N_2 must exceed N_1, which is population inversion. A laser must also

accomplish the extra feat of having stimulated emission rates exceed that of spontaneous emission and absorption, so $\varphi(v)$ must reach a critical level. Since hv is fixed, the only way to increase $\varphi(v)$ is to increase N_{ph}. The photon density of a coherent beam of radiation in a two-level lasing medium is subject to two competing processes: absorption and stimulated emission. The net loss of photon density per unit time is expressed as:

$$-hv\frac{dN_{ph}}{dt} = N_1\varphi(v)B_{12} - N_2\varphi(v)B_{21} = (N_1 - N_2)\varphi(v)B_{21} \Rightarrow \frac{dN_{ph}}{dt} = (N_2 - N_1)N_{ph}B_{21} \quad (3.7)$$

Again it is clear that in order for the number of photons in the coherent beam to increase and produce consistent lasing, N_2 must be larger than N_1. For electrically pumped devices, this is accomplished when the current density has reached a threshold value such that the value N_2 is large enough to overcome absorption and spontaneous emission. In a steady state, the change in N_2 is zero as each injected carrier spontaneously recombines (so that N_2 never reaches N_1). This is quantitatively described by the equation:

$$\frac{dN_2}{dt} = \frac{J}{qd} - \frac{N_2}{\tau} = 0 \quad (3.8)$$

where J is the injection current density, q is electron charge, d is the thickness of the lasing medium, and τ is the recombination rate. To overcome this steady state, the threshold electron density must be breached. The corresponding threshold injection current density to accomplish this is extracted from equation 3.8 and given by

$$J_{th} = \frac{qdN_{2,th}}{\tau} \tag{3.9}$$

The threshold current density is one of the primary figures of merit for a laser diode, the lower the better. It can be improved a number of ways, for example: quantum wells within the p-n junction enhance population inversion via quantum confinement, which in turn enhances stimulated emission. Thus quantum wells are often found in the structures of III-nitride laser diodes. A further discussion on the quantum mechanics of lasing action can be found in the literature [32-34].

3.2.2 Optical Confinement

In order to increase the probability of stimulated emission, photons can be confined within the diode, resonating back and forth making several passes over the active region, as opposed to being emitted directly following electron-hole recombination. This is done via optical waveguides on either side of the active region to confine photons in the transverse directions; the active region and waveguides must have different indices of refraction in order for reflection to occur at the interfaces. This ensures that the optical wave function is only subject to absorption losses within the active region. These losses are quantified by the absorption coefficient, defined as

$$\alpha = (N_1 - N_2)B_{21}\frac{n_r}{c} \tag{3.10}$$

where n_r is the refractive index, c is the speed of light, and N_1 and N_2 are carrier densities of E_1 and E_2, and B_{21} is the Einstein coefficient for stimulated emission. In order for stimulated emission to occur, this absorption must become negative, by making $N_2 > N_1$ as described previously. Under this condition, Equation 3.10 is negated and is redefined as gain where $g = -\alpha$. But if the optical wave function leaks from the active region into the surrounding layers, the absorption coefficients of those layers are added to that of the active region in an amount proportional to the amount of optical leakage. The result is that total absorption losses are increased, and threshold gain is more difficult to achieve.

In an edge-emitting laser, photons are also lost at the ends of the device. For an LED, this would be fine. However a laser by definition produces a coherent beam of light, which requires some confinement of the beam to make several passes through the active region resulting in more stimulated emission each time. The losses at these end boundaries are given by

$$\gamma = \frac{1}{2l}\ln\left(\frac{1}{R_1 R_2}\right) \tag{3.11}$$

where l is the length of the optical cavity, and R_1 and R_2 are the reflectivity at each end. Lateral optical confinement is achieved by cleaving the sides of the laser diode. The differences in refractive index at the air-semiconductor interface are sufficient to provide some reflection. This can be enhanced by the subsequent deposition of mirrors to the sides of the cleaved facets, which increase the values of R_1 and R_2.

The total threshold gain is a sum of the absorption losses within the optical cavity and transmission losses at the ends or $g_{th} = a + \gamma$. Thus good mirror facets, cladding, and

material quality are all essential in lowering the threshold current density required to achieve threshold gain and ultimately lasing.

3.2.3 Technical Challenges

Strain-Induced Defects

Due to the additional requirement of optical confinement, laser diodes are significantly more complex than light emitting diodes in both epitaxial structure and device fabrication. To enhance transverse optical confinement, the index of the cladding layers must be reduced as much as possible, and thus the bandgap must be extended as much as possible. A common way to do this is by surrounding the InGaN active regions with AlGaN. The drawback of this approach is the difference in lattice constant that accompanies bandgap as per Figure 1.2. If the resulting strain is too great, it can lead to crystal lattice relaxation, the product of which is a dislocation and/or cracking. These defects are non-radiative recombination centers and can strongly inhibit if not kill altogether the lasing potential of the diode.

The most common substrate for devices grown via MOCVD is sapphire due to its low cost and ready availability. However, the lattice mismatch between sapphire and GaN is large at around 13%. This leads to built-in strain in the epitaxial layers and increased formation of defects even with the low temperature buffers described previously. The added complexity of a laser diode structure – using GaN contacts, InGaN active regions, and AlGaN claddings, each with their own lattice constant – amplifies this strain problem. To eliminate the effect of the substrate mismatch, free-standing GaN substrates can be grown using hydride vapor phase epitaxy (HVPE). Growing GaN layers

on a GaN substrate is known as “homoepitaxy.” The result is a reduction in overall lattice strain in the device, which reduces the probability of relaxation and defect formation. A drawback of these free-standing GaN substrates is that they are slow and difficult to grow making the cost of each individual wafer quite high.

CHAPTER 4

GREEN LIGHT EMITTERS

4.1 Light Emitting Diode Design

The basic epitaxial structure of a III-nitride LED consists of an n-contact layer, the active region, and p-contact layer. Figure 4.1 shows this fundamental structure. Some designs will also include a large-bandgap electron blocking layer (EBL) between the active region and hole injection layer in order to prevent the flow of electrons into the p-region and contain recombination in the active region.

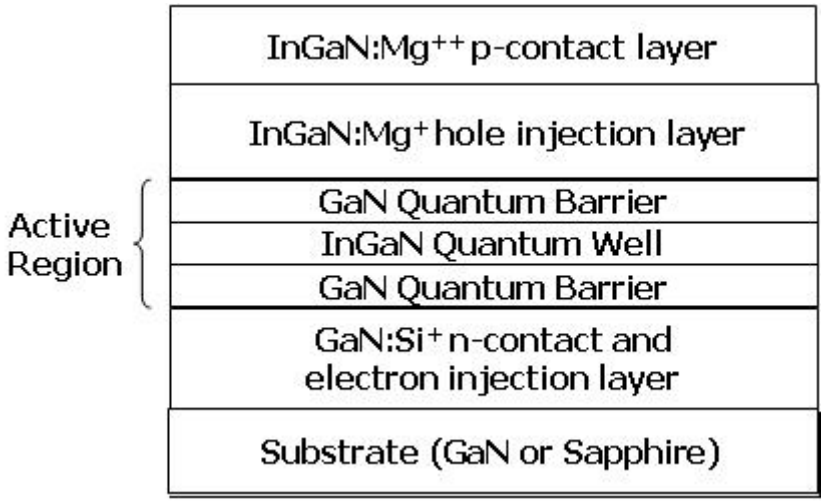

Figure 4.1: Epitaxial layer structure of a light emitting diode.

In order to minimize the effect of indium decomposition in the active region under high temperature p-layer growth, the top p-GaN contact and injection layers were replaced with p-$In_{0.04}Ga_{0.96}N$ [35, 36]. By using p-$In_{0.04}Ga_{0.96}N$, these top layers could be grown at a lower temperature, and thus become "active region friendly." A side-effect of

this method is the formation of V-defects and surface pits, which are paths of leakage current and centers for non-radiative recombination [37].

These further complications can be mitigated by the use of GaN substrates [38]. By employing homoepitaxial growth of GaN on free-standing GaN, the reduction in lattice mismatch at the substrate-epitaxial interface leads to a reduction in dislocation density. As can be seen in Figure 4.2, switching the substrate from sapphire to GaN reduces the surface dislocation density of LED structures from ~$1.0x10^9$ cm^{-2} to $1.4x10^7$ cm^{-2}.

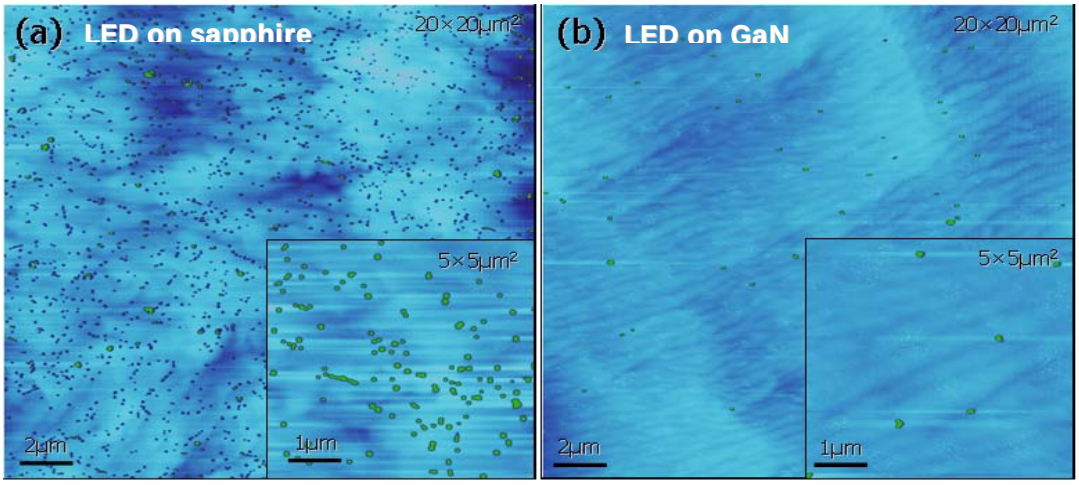

Figure 4.2: AFM images of LED structure on (a) sapphire and (b) GaN substrate. The pit density is reduced from ~$1.0x10^9$ cm^{-2} to $1.4x10^7$ cm^{-2} by switching to free-standing GaN substrate.

4.2 Light Emitting Diode Device Data

LEDs were grown on (0001) sapphire and (0001) free-standing GaN substrate via MOCVD on a 6x2" Thomas Swan reactor with a close-coupled showerhead as described previously. EpiPure™ trimethylgallium (TMGa) and trimethylindium (TMIn) were used as alkyl precursors and ammonia (NH_3) as the hydride precursor. Silane (SiH_4) was used

as the n-type dopant and bis-cyclopentadienyl magnesium (Cp_2Mg) was used for p-type doping.

The exact epitaxial structure on free-standing GaN substrates was as follows: a Si-doped GaN layer (n = $5x10^{18}$ cm^{-3}, 1.5 μm), a 5-period InGaN/GaN (2.5 nm/10 nm) multiple quantum well (MQW) active region, a p-$In_{0.04}Ga_{0.96}N$:Mg hole injection layer (100 nm), and finally a heavily doped $In_{0.04}Ga_{0.96}N$:Mg contact layer (20 nm). Hydrogen was used as carrier gas for the n-type injection layers and was switched to nitrogen for the MQWs and p-layers. The structure on sapphire is the same except for an extra 2 μm GaN:Si template layer grown on the substrate via two-step strained heteroepitaxy with low-temperature buffer layer followed by high temperature 2D growth.

The wafer was fabricated into devices with square geometry 350 x 350 μm^2 mesas defined by inductively-coupled plasma (ICP) etching. Ti/Al/Ti/Au n-type contacts were deposited via electron-beam evaporation and annealed at 700 °C. Ni/Au p-type contacts were then deposited and annealed at 600 °C in an oxygen ambient to achieve ohmic contact.

Figure 4.3 shows the PL spectra of the LED epitaxial structure grown on a sapphire and on a GaN substrate. The peak wavelengths are 523 nm and 528 nm for the LED on sapphire and GaN respectively, with dominant emission coming from the InGaN MQWs. Although the LED on sapphire has dislocation density which is ~2 orders of magnitude larger than that on GaN, the peak intensities are similar. This is due to the relative insensitivity of InGaN/GaN MQWs to dislocations at low excitation levels. The FWHM is 42.2 nm for the LED on GaN and 51.9 nm for the LED on sapphire. The

linewidth broadening on sapphire is associated with the higher dislocation density and resulting indium segregation as described earlier.

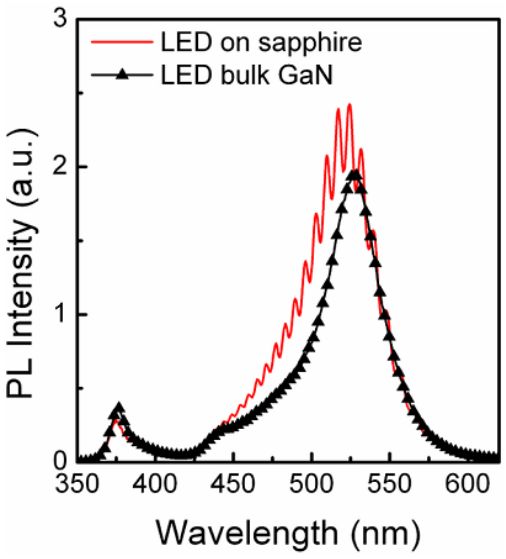

Figure 4.3: Photoluminescence spectra of green LEDs grown on free-standing GaN and sapphire substrates.

Figure 4.4 shows the EL spectra of fully fabricated LEDs on sapphire and GaN substrate. The wafer-level (unpackaged) EL was obtained through the top-side, semi-transparent p-type contact. Both samples show comparable peak intensities. The FWHMs are also similar, with 30 nm for the LED on GaN and 33.8 nm for the LED on sapphire. The device size in the EL measurement is much smaller than the laser spot size for the PL measurement, thus reducing the broadening effects of indium fluctuation.

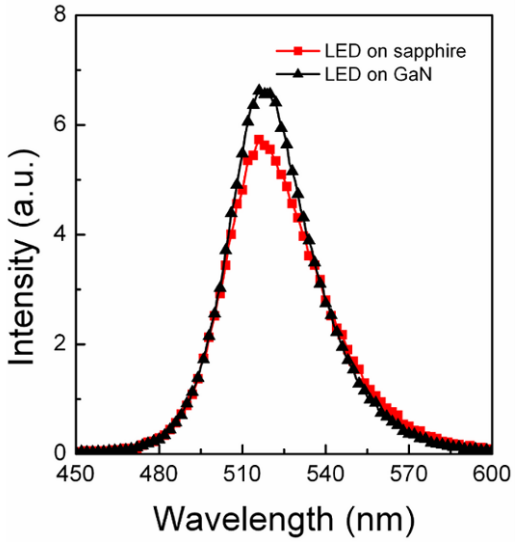

Figure 4.4: Electroluminescence spectra of green LEDs grown on free-standing GaN and sapphire substrates at a current of 20 mA.

A more telling example of the difference between the LEDs on GaN and sapphire are the reverse leakage currents which are heavily influenced by defects [39]. Figure 4.5 demonstrates the reverse current-voltage characteristics of both structures. The reverse-current for the LED on free-standing GaN is lower than the measurement limit up to -4 Volts and then two orders of magnitude below that of the LED on sapphire from -4 Volts onwards. This correlates to the two order of magnitude reduction in dislocation density resulting from homoepitaxial growth on free-standing GaN as opposed to heteroepitaxial growth on the non-native sapphire substrate. This lower reverse leakage current may be beneficial to the long-term reliability of green LEDs by the reduction excess heat resulting from non-radiative recombination at the defect sites.

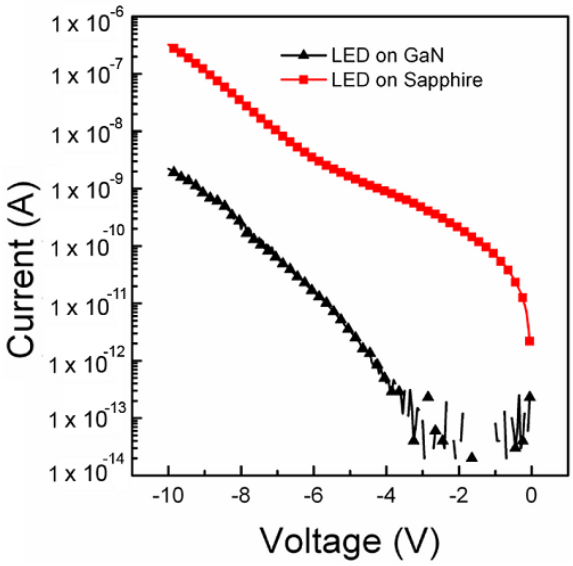

Figure 4.5: Reverse current–voltage curves for LEDs grown on free-standing GaN substrate and sapphire substrate.

Since free-standing GaN substrates currently are relatively expensive, it is important to develop methods for reducing surface pit density on sapphire. The origins of these pits have been reported to be from strain relaxation and the formation of threading dislocations, and kinetic effects of layer growth [40, 41]. Conventional LED structures using p-GaN contact layers benefit from the higher surface diffusivity of Ga adatoms in GaN:Mg, (even at the lower growth temperature) as compared to InGaN:Mg, thus no surface pits are observed. The formation of these surface pits in p-InGaN layers implies that they are derived from dislocations in the p-InGaN layer itself. Thus the inclusion of a GaN:Mg layer in a p-contact layer can reduce pit formation. One way to do this is by using a graded alloy composition p-$In_xGa_{1-x}N$:Mg layer with indium composition going from x = 4% to 0%, with the very top serving as a p-GaN planarization layer. This graded layer was used in an LED grown on sapphire in place of the 120 nm free-standing p-InGaN hole injection and contact layers, and grading was accomplished by ramping the

growth temperature from 840 ºC to 930 ºC from right after the last quantum barrier to the surface. This method reduced the pit density from ~1 x 10^9 cm^{-2} to ~3 x 10^8 cm^{-2} as shown by the SEM image in Figure 4.6.

Another option is to use a short period superlattice (SPSL) of alternating p-InGaN and p-GaN layers of 2.5nm each for a total of 120 nm to replace the standard p-InGaN injection and contact players. The p-GaN layers serve as strain reduction and planarization layers, and reduced the pit density further to ~1x$10^8$$cm^{-2}$ as is demonstrated by the AFM image in Figure 4.7.

The LEDs with SPSL p-type layers were fabricated the same as before. Figure 4.8 shows the reverse bias characteristics of LEDs grown on sapphire with conventional p-InGaN and with SPSL p-InGaN/GaN injection and contact layers. As in the case with the use of free-standing GaN substrates, the reduction in pit density via the use of the SPSL also reduces the reverse bias current by nearly one order of magnitude.

However, the improvement in electrical characteristics came with a slight trade-off in optical performance as is seen in Figure 4.9. The slight reduction in EL intensity in the sample with SPSL p-contact layers may be due to the differences in refractive index between p-InGaN and p-GaN, as some light would be reflected at each interface.

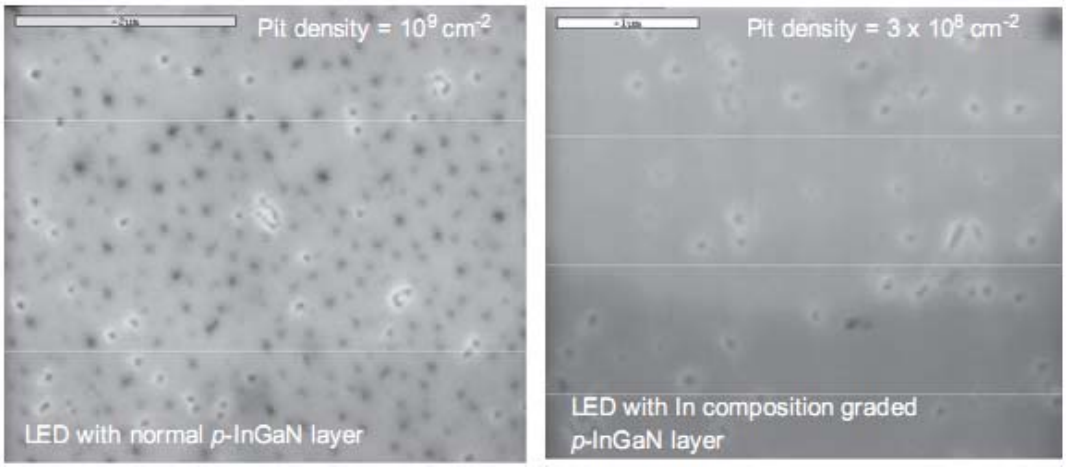

Figure 4.6: SEM images of the epitaxial structure surfaces of green LEDs with (a) a p-$In_{0.04}Ga_{0.96}N$ layer and (b) a p-$In_xGa_{1-x}N$ graded-composition layer grown on sapphire substrate.

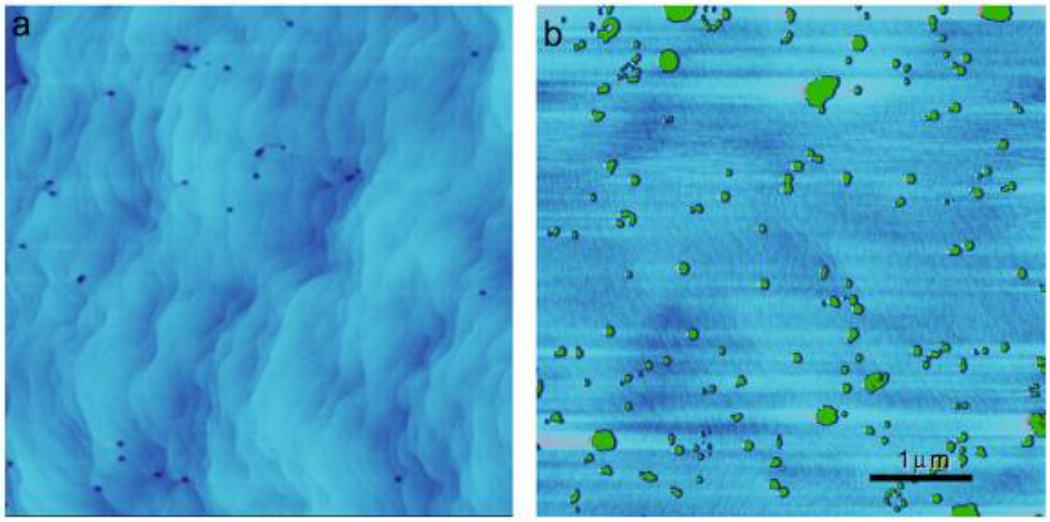

Figure 4.7: AFM images of the epitaxial structure surfaces of green LEDs with (a) p-InGaN:Mg/GaN:Mg SPSL and (b) a p-$In_{0.04}Ga_{0.96}N$ layer grown on sapphire substrates.

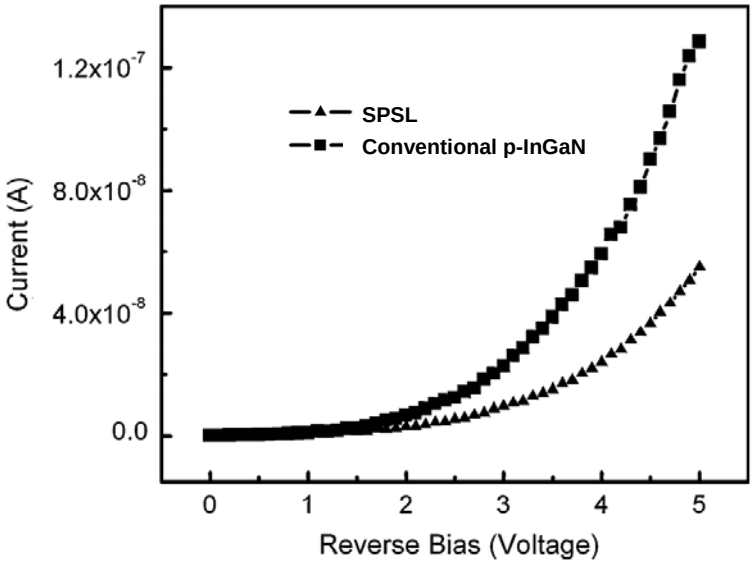

Figure 4.8: Reverse bias current of an LED with conventional p-InGaN and SPSL InGaN:Mg/GaN:Mg hole injection and contact layers.

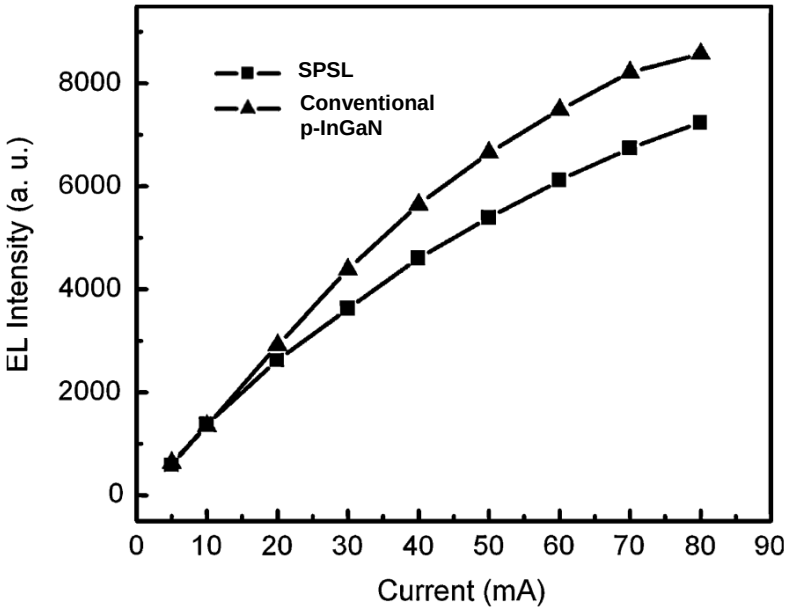

Figure 4.9: Electroluminescence intensity of an LED with conventional p-InGaN and SPSL InGaN:Mg/GaN:Mg hole injection and contact layers.

4.3 Laser Diode Design

The basic epitaxial structure of a III-nitride LD consists of an n-contact layer, an n-cladding layer, n-side waveguide, active region, electron blocking layer, p-side waveguide, p-cladding layer, and p-contact layer. Growth of LDs is more complicated than that of LEDs due to the added complexities of the cladding and waveguide layers. Figure 4.10 shows the fundamental structure of a III-N semiconductor laser.

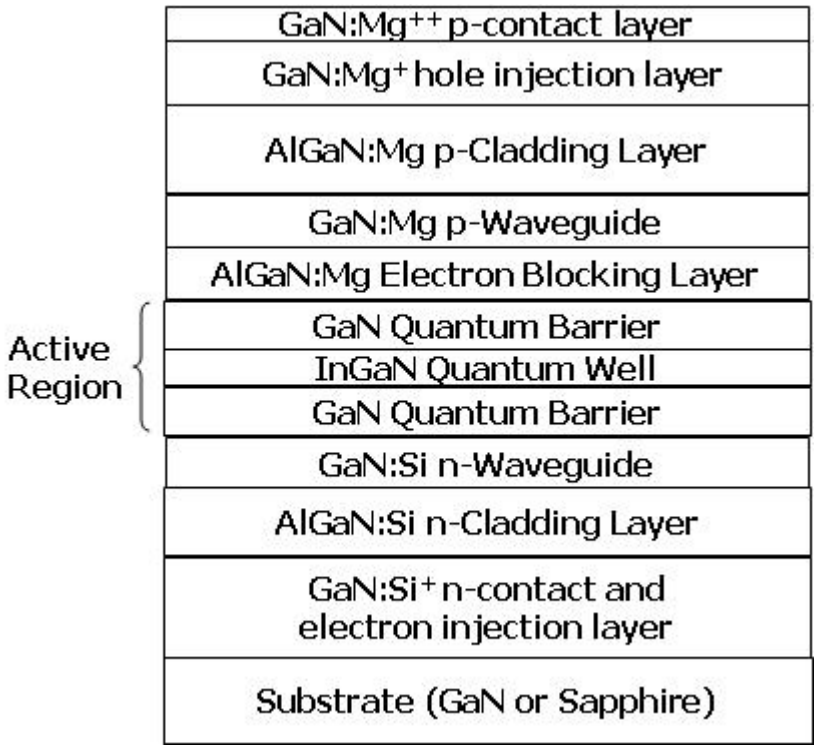

Figure 4.10: Epitaxial structure of a III-N laser diode.

The lattice mismatch between GaN and AlGaN leads to strain in the crystal lattice of each layer. If this strain becomes too great, relaxation will occur and can form a dislocation and for thicker layers, the strain can lead to cracking. The dislocations act as non-radiative recombination centers and paths for leakage current and can effectively kill

device performance. In these LD structures, conventional AlGaN layers were replaced with AlGaN-GaN short-period superlattice layers to eliminate cracking. Since the short periods of the superlattice are far thinner than the critical thickness for dislocation formation, AlGaN can be included in the structure without the formation of cracks. Figure 4.11 shows spontaneous EL measurements of two LD structures. The first has conventional constant alloy composition AlGaN cladding layers with thicknesses of 300 nm for the p-cladding and 400 nm for the n-cladding respectively. The other LD structure has AlGaN/GaN SPSL cladding layers with 90 pairs of 2.5/2.5 nm AlGaN:Mg/GaN:Mg for p-cladding and 150 pairs of 2.3/2.3 nm AlGaN:Si/GaN:Si for the n-cladding. The intensity is substantially higher for the sample with SPSL cladding layer, owing to the reduction in cracks and also dislocations and point defects.

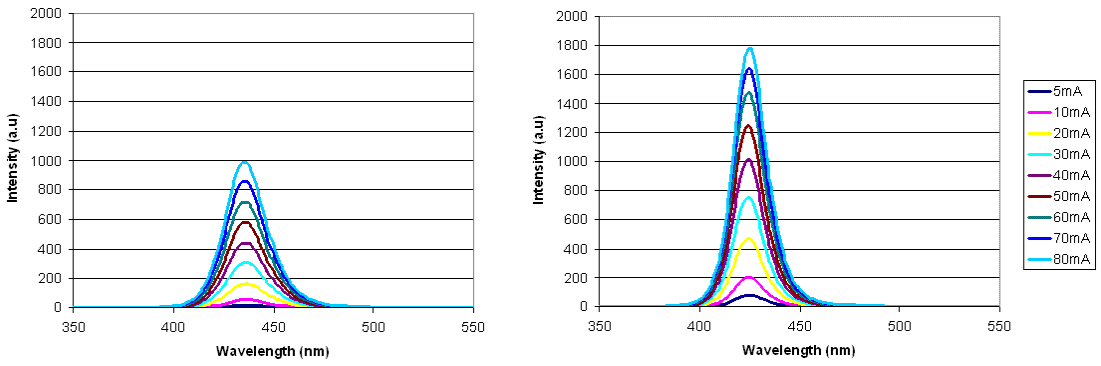

Figure 4.11: EL quick test measurement of LD structure with (a) conventional AlGaN cladding and (b) SPSL AlGaN/GaN cladding layers.

As described previously, excess magnesium can cause layer degradation due to overdoping. Thus the Cp_2Mg flow must be carefully optimized for p-layer growth, especially for relatively thick layers such as the SPSL p-type cladding layer. Figures 4.12 and 4.13 show the optimization curves for magnesium doping in the SPSL p-cladding

layers. Resistivity was measured via Hall measurement for several individually grown p-cladding layers, identical to that of the LD structure, but with various Cp_2Mg flow rates. The spontaneous emission of full LD structures with the different p-cladding layers was measured via EL. The optimized flow rate was found to be 100 sccm.

With this optimized condition for the SPSL p-cladding layer, the over material quality of the LD structures was significantly improved. Figure 4.14 shows surface images of two LD samples taken with an optical microscope. The non-optimized structure shows several cracks. The LD structure with optimized SLs is crack free.

To further reduce strain in the LD structure, sapphire substrate was replaced with a free-standing GaN substrate, as was done with the LEDs. Homoepitaxial growth relieves substrate-epitaxial layer lattice mismatch and thus lattice strain as well. Strain reduction reduces the probability of strain relaxation and dislocation formation, and improves the performance of optical devices. It also reduces the effects of strain-induced piezoelectric effects such as the QCSE.

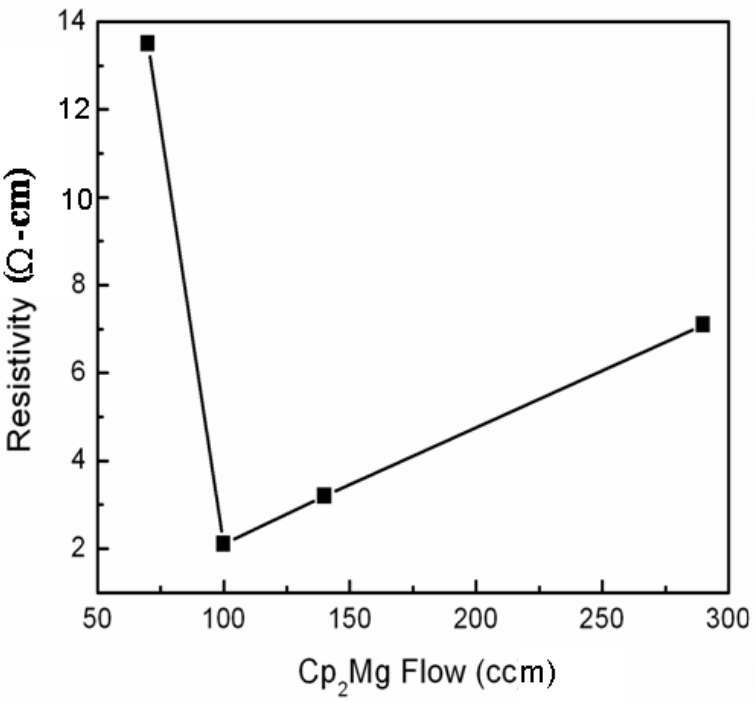

Figure 4.12: Resistivities of several AlGaN:Mg/GaN:Mg short-period superlattices grown with different Cp_2Mg flow rates.

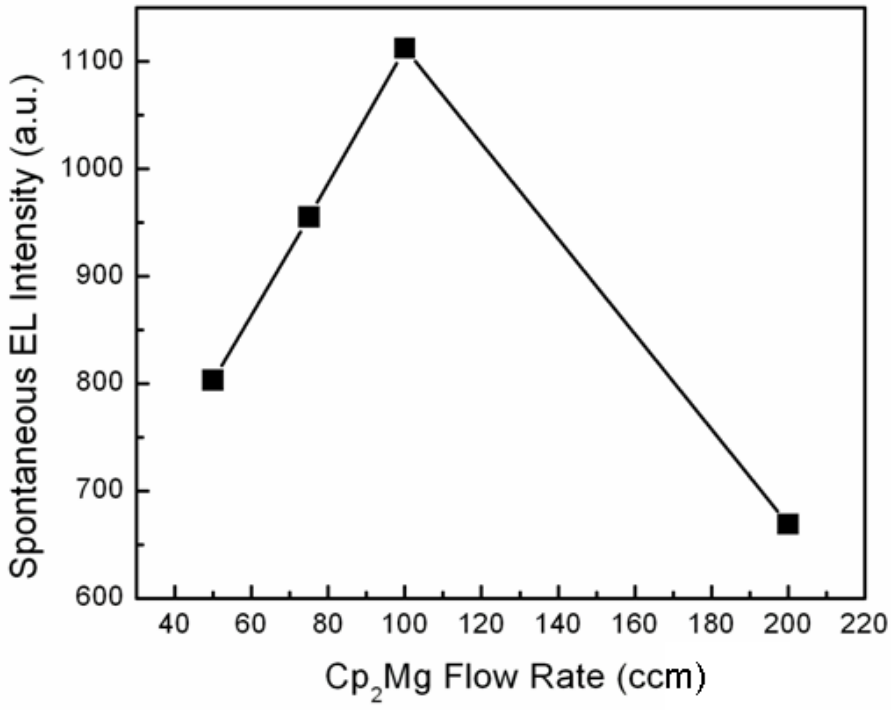

Figure 4.13: Spontaneous EL intensities of several LD structures with AlGaN:Mg/GaN:Mg short-period superlattices grown at different Cp_2Mg flow rates.

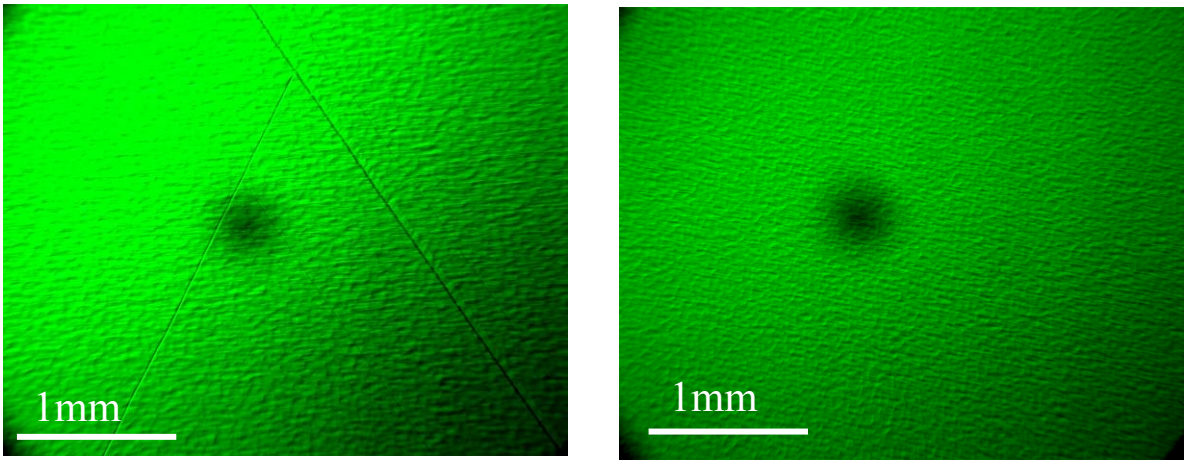

Figure 4.14: Surface images of full LD structures grown on sapphire with (a) non-optimized SPSLs and (b) optimized SPSL layers.

4.4 Laser Diode Device Data

LD samples were grown on (0001) free-standing GaN substrates to take advantage of the lower dislocation density associated with homoepitaxial growth. This serves to increase chances of achieving lasing action at low threshold current densities in the final device. EpiPure^{TM} trimethylgallium (TMGa), trimethylindium (TMIn), and trimethylaluminum (TMAl) were used as alkyl precursors and ammonia (NH_3) as the hydride precursor. Silane (SiH_4) was used for n-type doping and bis-cyclopentadienyl magnesium (Cp_2Mg) was used for p-type doping.

The exact epitaxial structure for our basic LD was as follows: a Si-doped GaN layer (n= $5x10^{18}$ cm^{-3}, 3 μm), a 150-period $Al_{0.16}Ga_{0.84}N$:Si/GaN:Si (2.5 nm/2.5 nm) SPSL n-cladding layer, a 100 nm GaN:Si n-waveguide, a 2-period InGaN/GaN:Si (2.8 nm/8.8 nm) MQW active region, an 8.8 nm GaN:ud spacer layer, a 20 nm $Al_{0.18}Ga_{0.82}N$:Mg electron blocking layer, 100 nm GaN:Mg p-waveguide, 90 period $Al_{0.16}Ga_{0.84}N$:Mg/GaN:Mg (2.5 nm/2.5 nm) SPSL p-cladding layer, 30 nm GaN:Mg hole injection layer, and a heavily doped 20 nmGaN:Mg contact layer. Several test samples will also be discussed below, which were grown on (0001) c-plane sapphire substrate with the same configuration unless otherwise noted.

The LD wafers were fabricated into ridge-waveguide laser diodes. Stripe-geometry mesas with various widths (2-12 μm) were defined using inductively-coupled plasma reactive ion etching (ICP-RIE) using silicon dioxide as an etch mask to partially etch the p-cladding layer. Then, an aluminum oxide (Al_2O_3) passivation/lateral optical confinement layer was deposited. A buffered-oxide etch was then performed to selectively remove the SiO_2 etch mask, followed by p-ohmic contact deposition

consisting of Ni/Ag/Pt annealed in oxygen at 500 °C. The backside of the wafers were lapped and polished to thin the free-standing GaN substrate. Electron-beam deposition was used to deposit Ti/Al n-ohmic contacts to the N-face n-GaN layer. Finally, the laser facet was formed by cleaving along the $(11\bar{2}0)$ m-plane, followed by the deposition of a high-reflection coating consisting of five- and three- pairs of quarter wavelength SiO_2/TiO_2 dielectric stacks deposited on the back and front facets, respectively.

In an effort to reduce strain in the active region, the GaN waveguides were augmented with $In_{0.03}Ga_{0.97}N$ waveguides. It was hoped that these InGaN layers would be more closely lattice-matched to the InGaN of the active region and reduce strain if the lower waveguide was partially or fully relaxed, resulting in mitigation or even elimination of strain-induced polarization fields and associated QCSE. It was also theorized that the larger difference in refractive index between $In_{0.03}Ga_{0.97}N$ and GaN at 450-500 nm should serve to the advantage of optical confinement [42, 43]. In terms of device structure, 80 nm undoped $In_{0.03}Ga_{0.97}N$ waveguides were grown directly before and after the active region.

Figure 4.15 compares the electroluminescence measurements of spontaneous emission properties of LD samples grown with only GaN waveguides (WGs) and with the augmented InGaN waveguide structure. The EL intensity of the InGaN waveguide structure increases much faster with input current than that of the GaN waveguide structure. At 80 mA the intensity is nearly doubled. The FWHM has also been reduced by about 6 nm.

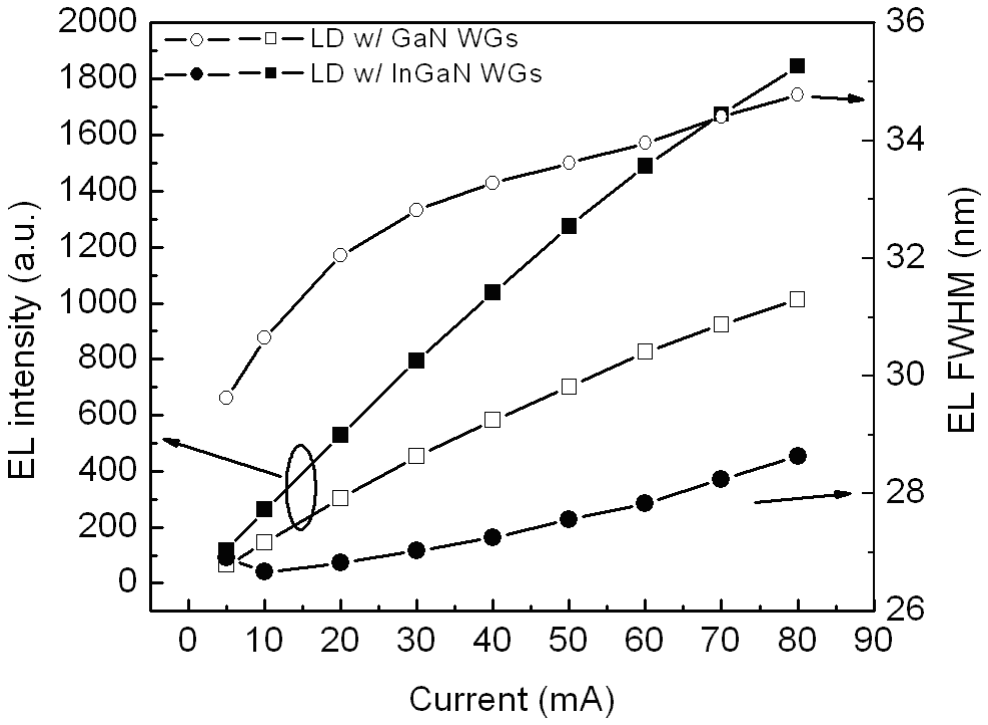

Figure 4.15: Spontaneous EL intensity and FWHMs of LD structures with GaN waveguides and with $In_{0.03}Ga_{0.97}N$ waveguides.

Figure 4.16 shows the reciprocal space maps (RSMs) produced by XRD for LD samples with InGaN waveguides grown on sapphire and GaN substrate. The intensity peaks corresponding to the InGaN waveguides vertically aligns with those of the AlGaN cladding layer and substrate for each sample, indicating that the InGaN waveguides (and also the active region) are still fully strained to the substrate. It is instructive to note that the FWHM of the omega scan is significantly reduced in the RMS for the sample grown on GaN substrate compared to that on sapphire. This is attributed to the reduced dislocation density associated with homoepitaxial growth.

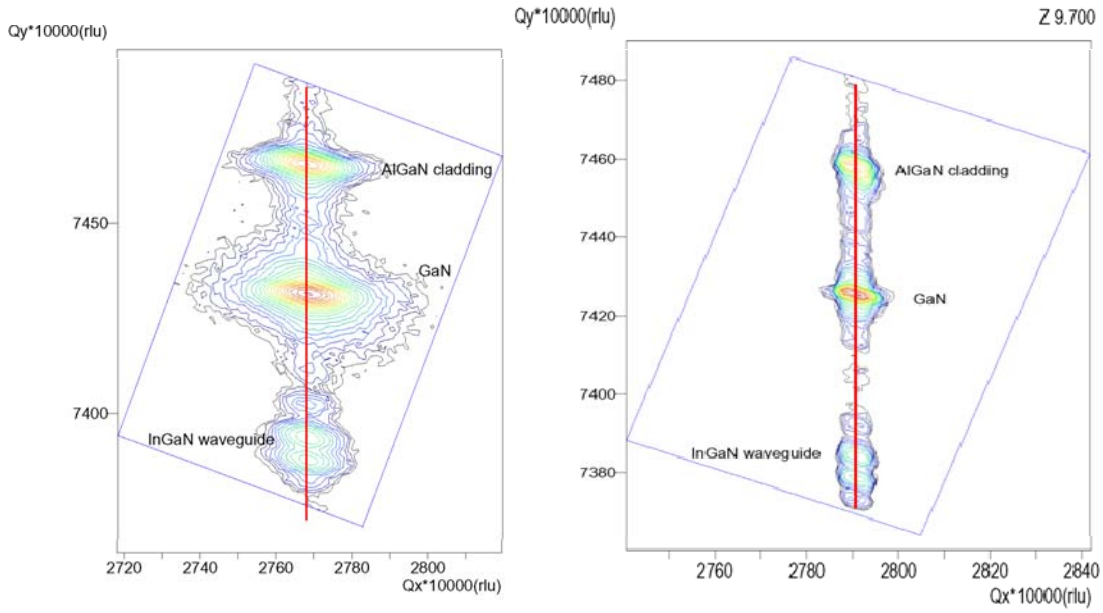

Figure 4.16: High Resolution-XRD reciprocal space mappings around the (105) spot of LD structures with In0.03Ga0.97N waveguides grown on (a) sapphire substrate and (b) GaN substrate.

So while no strain reduction took place, an explanation for the improvement in EL may be that undoped InGaN blocks the diffusion of Mg from the top p-type layers back down into the active region during high-temperature p-layer growth, since magnesium more readily diffuses through GaN than it does InGaN. A SIMS profile analysis (Figure 4.17) shows the limited back diffusion of Mg into the active region, barely higher than background levels.

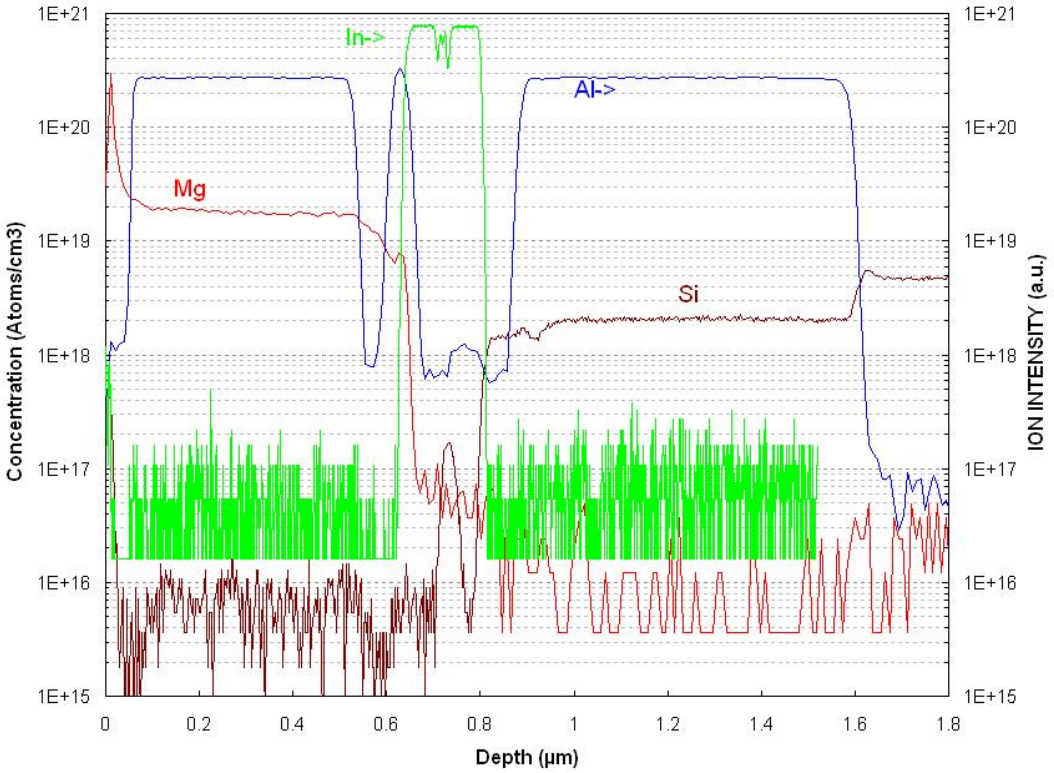

Figure 4.17: SIMS analysis of the LD epitaxial layers. The p-side InGaN waveguide starts at ~0.7 µm.

Figure 4.18 shows the lasing spectra for a fully fabricated LD with InGaN waveguides grown on a free-standing GaN substrate. The laser was measured under room-temperature pulsed operation with a pulse width of 1 µs at 1 kHz frequency. The peak wavelength is 454.6 nm with a FWHM of 0.5 nm. Figure 4.19 shows the light-output power and operating voltage versus current density for the device. The threshold current density is 3.3 kA/cm^2 and the threshold voltage is 5.9 Volts.

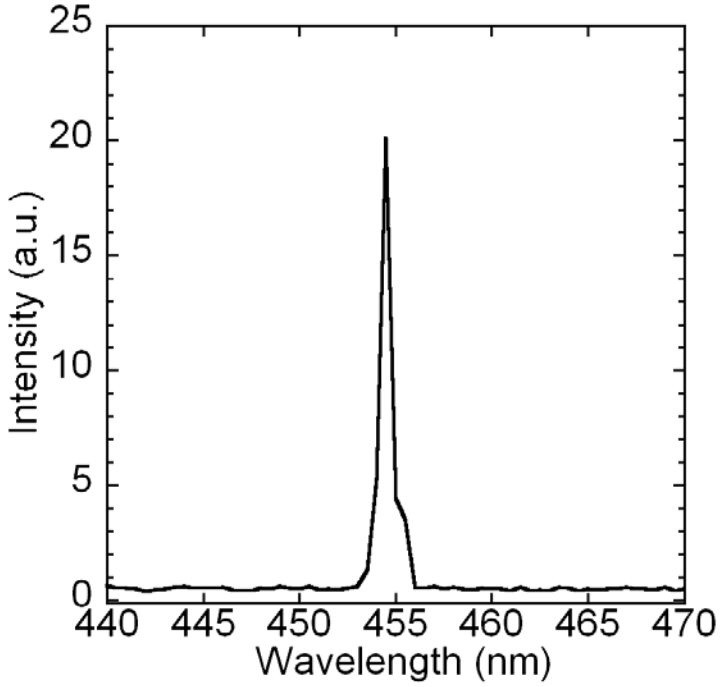

Figure 4.18: Lasing spectra of 454.6 nm laser.

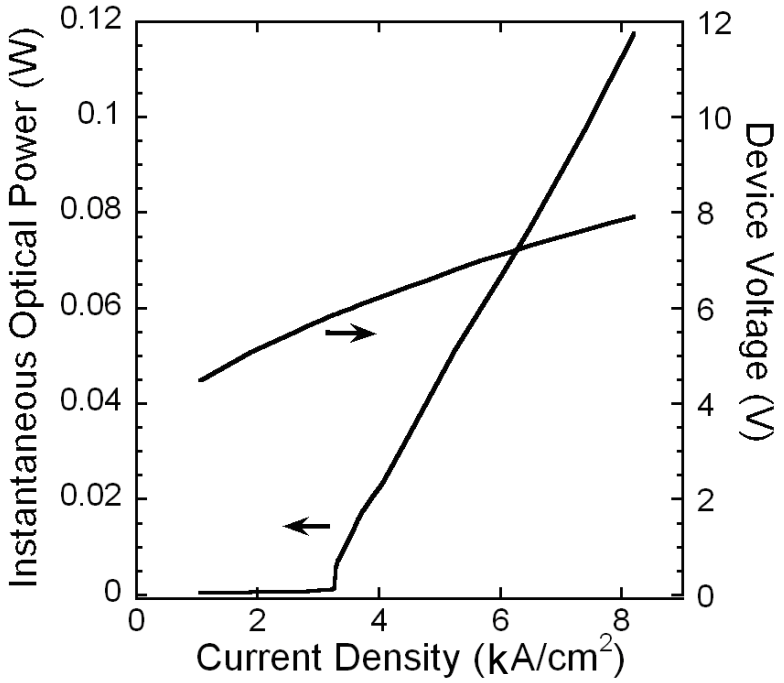

Figure 4.19: Voltage and light output versus current density for a fully fabricated 454.6 nm laser with $In_{0.03}Ga_{0.97}N$ waveguides.

CHAPTER 5

CONCLUSION AND FUTURE WORK

A review of the fundamentals of III-nitride materials and metalorganic chemical vapor deposition were presented and the characterization techniques employed in this thesis were described. The basics of InGaN LEDs and LDs were discussed along the technical challenges involved in their evolution.

Several green LEDs were developed using different epitaxial structures and substrates. The dislocation density of the material layers was reduced from ~1.0 x 10^9 cm^{-2} to 1.4 x 10^7 cm^{-2} by switching from sapphire to free-standing GaN substrates, as measured by atomic force microscopy. The full-width half maximums of the emission from the LEDs on sapphire and GaN were 51.9 nm and 42.2 nm, respectively, as measured by photoluminescence, and 33.8 nm and 30 nm, respectively, measured from device level electroluminescence. The LED on GaN exhibited a reverse-leakage current two orders of magnitude lower than its counterpart on sapphire, attributed to the reduced dislocation density.

To reduce the defect density and improve the performance of green LEDs, alternative structures were developed to reduce the defect density. A graded-composition InGaN:Mg p-layer design reduced the defect density from ~1 x 10^9 cm^{-2} to 3 x 10^8 cm^{-2}. The use of a p-InGaN/p-GaN superlattice hole injection and contact layer further reduced the defect density to 1x$10^8$$cm^{-2}$. The reverse leakage current for the superlattice p-layer structure was reduced by one order of magnitude as compared to the control sample, but saw a decrease in EL intensity.

An LD structure emitting in the blue region of the spectrum at 454 nm was developed. The p-cladding layer was optimized by replacing conventional constant-alloy-

composition AlGaN with an AlGaN/GaN superlattice and determining the ideal p-type doping level. As a result, strain relaxation and crack formation were virtually eliminated.

In an effort to reduce the overall strain in the active region, thereby mitigating the quantum-confined Stark effect, the GaN waveguides were augmented with InGaN waveguides. While no evidence of strain reduction was directly measured, the LD structure with InGaN waveguides exhibited an enhanced spontaneous EL intensity and reduced FWHM. This structure was fabricated into ridge-guided laser diodes, and the lasing wavelength of the LDs was 454.6 nm with a FWHM of ~0.5 nm. The lowest threshold current density was ~3.3 kA/cm^2 and the threshold voltage was 5.9 Volts.

Future experiments will seek to improve the quality of LED structures by optimizing the electron blocking layer (EBL) and active region. For example, strain can be further reduced by utilizing a lattice-matched, wide-bandgap InAlN layer for the EBL. The wavelength of future LD structures will be further pushed towards 500 nm (blue-green) and beyond via strain and polarization engineering.

REFERENCES

[1] M. R. Krames, O. B. Shchekin, R. Mueller-Mach, G. Mueller, L. Zhou, G. Harbers, and M. G. Craford, "Status and Future of High-Power Light-Emitting Diodes for Solid-State Lighting," *J. Display Technol.,* vol. 3, pp. 160-175, 2007.

[2] G. Binnig, C. Quate, and C. Gerber, "Atomic force microscope," *Physical Review Letters,* vol. 56, pp. 930-933, 1986.

[3] J. N. Holonyak and S. F. Bevacqua, "Coherent (Visible) Light Emission From $Ga(A_{1-x}P_x)$ Junctions," *Applied Physics Letters,* vol. 1, pp. 82-83, 1962.

[4] S. Nakamura, T. Mukai, and M. Senoh, "Candela-class high-brightness InGaN/AlGaN double-heterostructure blue-light-emitting diodes," *Applied Physics Letters,* vol. 64, pp. 1687-1689, 1994.

[5] S. Nakamura, M. Senoh, S.-i. Nagahama, N. Iwasa, T. Yamada, T. Matsushita, H. Kiyoku, and Y. Sugimoto, "InGaN-Based Multi-Quantum-Well-Structure Laser Diodes," *Japanese Journal of Applied Physics,* vol. 35, p. L74, 1996.

[6] H. P. Maruska and J. J. Tietjen, "The Preparation and Properties of Vapor-Deposited Single Crystalline GaN," *Applied Physics Letters,* vol. 15, pp. 327-329, 1969.

[7] H. M. Manasevit, F. M. Erdmann, and W. I. Simpson, "The Use of Metalorganics in the Preparation of Semiconductor Materials," *Journal of The Electrochemical Society,* vol. 118, pp. 1864-1868, 1972.

[8] H. Amano, N. Sawaki, I. Akasaki, and Y. Toyoda, "Metalorganic vapor phase epitaxial growth of a high quality GaN film using an AlN buffer layer," *Applied Physics Letters,* vol. 48, pp. 353-355, 1986.

[9] S. Nakamura, T. Mukai, and M. Senoh, "Si- and Ge-Doped GaN Films Grown with GaN Buffer Layers," *Japanese Journal of Applied Physics,* vol. 31, p. 2883, 1992.

[10] S. Nakamura, N. Iwasa, M. Senoh, and T. Mukai, "Hole Compensation Mechanism of P-Type GaN Films," *Japanese Journal of Applied Physics,* vol. 31, p. 1258, 1992.

[11] H. Amano, M. Kito, K. Hiramatsu, and I. Akasaki, "P-Type Conduction in Mg-Doped GaN Treated with Low-Energy Electron Beam Irradiation (LEEBI)," *Japanese Journal of Applied Physics,* vol. 28, p. L2112, 1989.

[12] S. Nakamura, T. Mukai, M. Senoh, and N. Iwasa, "Thermal Annealing Effects on P-Type Mg-Doped GaN Films," *Japanese Journal of Applied Physics,* vol. 31, p. L139, 1992.

[13] H. M. Manasevit, "Single-Crystal Gallium Arsenide on Insulating Substrates," *Applied Physics Letters,* vol. 12, pp. 156-159, 1968.

[14] R. D. Dupuis, P. D. Dapkus, R. D. Yingling, and L. A. Moudy, "High-efficiency GaAlAs/GaAs heterostructure solar cells grown by metalorganic chemical vapor deposition," *Applied Physics Letters,* vol. 31, pp. 201-203, 1977.

[15] R. D. Dupuis, P. D. Dapkus, J. N. Holonyak, E. A. Rezek, and R. Chin, "Room-temperature laser operation of quantum-well Ga[sub (1 - x)]Al[sub x]As-GaAs laser diodes grown by metalorganic chemical vapor deposition," *Applied Physics Letters,* vol. 32, pp. 295-297, 1978.

[16] Y. Ohba and A. Hatano, "A study on strong memory effects for Mg doping in GaN metalorganic chemical vapor deposition," *Journal of Crystal Growth,* vol. 145, pp. 214-218, 1994.

[17] S. Nakamura and T. Mukai, "High-Quality InGaN Films Grown on GaN Films," *Japanese Journal of Applied Physics,* vol. 31, p. L1457, 1992.

[18] L. van der Pauw, "A method of measuring specific resistivity and hall effect of discs of arbitrary shape," *Phillips Research Reports,* vol. 13, pp. 1-9, 1958.

[19] B. Heying, X. H. Wu, S. Keller, Y. Li, D. Kapolnek, B. P. Keller, S. P. DenBaars, and J. S. Speck, "Role of threading dislocation structure on the x-ray diffraction peak widths in epitaxial GaN films," *Applied Physics Letters,* vol. 68, pp. 643-645, 1996.

[20] C. Ryang Wie, "High resolution x-ray diffraction characterization of semiconductor structures," *Materials Science and Engineering: R: Reports,* vol. 13, pp. 1-56, 1994.

[21] B. D. Cullity, *Elements of x-ray diffraction*, 2d ed. ed. Reading, Massachusetts: Addison-Wesley Pub. Co., 1978.

[22] B. E. Warren, *X-ray diffraction*. Reading, Massachusetts: Addison-Wesley Pub. Co., 1969.

[23] J.-H. Ryou, P. D. Yoder, J. Liu, Z. Lochner, H. Kim H., S. Choi, H.-J. Kim, and R. D. Dupuis, "Control of Quantum-Confined Stark Effect in InGaN-Based Quantum Wells," *Selected Topics in Quantum Electronics, IEEE Journal of,* vol. 15, pp. 1080-1091, 2009.

[24] C. Yuan, T. Salagaj, W. Kroll, R. Stall, M. Schurman, C. Hwang, Y. Li, W. Mayo, Y. Lu, S. Krishnankutty, and R. Kolbas, "Effect of shroud flow on high quality InxGa1−xN deposition in a production scale multi-wafer-rotating-disc reactor," *Journal of Electronic Materials,* vol. 25, pp. 749-753, 1996.

[25] F. Scholz, V. Härle, F. Steuber, H. Bolay, A. Dörnen, B. Kaufmann, V. Syganow, and A. Hangleiter, "Low pressure MOVPE of GaN and GaInN/GaN heterostructures," *Journal of Crystal Growth,* vol. 170, pp. 321-324, 1997.

[26] J. P. Liu, Y. T. Wang, H. Yang, D. S. Jiang, U. Jahn, and K. H. Ploog, "Investigations on V-defects in quaternary AlInGaN epilayers," *Applied Physics Letters,* vol. 84, pp. 5449-5451, 2004.

[27] Y. C. Shen, G. O. Mueller, S. Watanabe, N. F. Gardner, A. Munkholm, and M. R. Krames, "Auger recombination in InGaN measured by photoluminescence," *Applied Physics Letters,* vol. 91, p. 141101, 2007.

[28] M.-H. Kim, M. F. Schubert, Q. Dai, J. K. Kim, E. F. Schubert, J. Piprek, and Y. Park, "Origin of efficiency droop in GaN-based light-emitting diodes," *Applied Physics Letters,* vol. 91, p. 183507, 2007.

[29] J. Xie, X. Ni, Q. Fan, R. Shimada, U. Ozgur, and H. Morkoc, "On the efficiency droop in InGaN multiple quantum well blue light emitting diodes and its reduction with p-doped quantum well barriers," *Applied Physics Letters,* vol. 93, p. 121107, 2008.

[30] A. A. Efremov, N. I. Bochkareva, R. I. Gorbunov, D. A. Lavrinovich, Y. T. Rebane, D. V. Tarkhin, and Y. G. Shreter, "Effect of the joule heating on the quantum efficiency and choice of thermal conditions for high-power blue InGaN/GaN LEDs," in *Semiconductors*. vol. 40: Springer Science & Business Media B.V., 2006, pp. 605-610.

[31] B. Monemar and B. E. Sernelius, "Defect related issues in the ``current roll-off'' in InGaN based light emitting diodes," *Applied Physics Letters,* vol. 91, p. 181103, 2007.

[32] P. Bhattacharya, *Semiconductor optoelectronic devices*. Englewood Cliffs, New Jersey: Prentice Hall, 1994.

[33] T. Suhara, *Semiconductor laser fundamentals*. New York, New York: Marcel Dekker, 2004.

[34] K. F. Brennan, *The physics of semiconductors : with applications to optoelectronic devices*. Cambridge, Massachusetts: Cambridge University Press, 1999.

[35] J. Limb, W. Lee, J. Ryou, D. Yoo, and R. Dupuis, "Comparison of GaN and In0.04Ga0.96N p -Layers on the Electrical and Electroluminescence Properties of Green Light Emitting Diodes," *Journal of Electronic Materials,* vol. 36, pp. 426-430, 2007.

[36] W. Lee,, J. Lim, J.-H. Ryou, D. Yoo,, M. A. Ewing, Y. Korenblit, and R. D. Dupuis, "Nitride-Based Green Light-Emitting Diodes With Various p-Type Layers," *Display Technology, Journal of,* vol. 3, pp. 126-132, 2007.

[37] J. Liu, J.-H. Ryou, Z. Lochner, J. Limb, D. Yoo, R. D. Dupuis, Z. Wu, A. M. Fischer, and F. A. Ponce, "Surface morphology control of green LEDs with p-InGaN layers grown by metalorganic chemical vapor deposition," *Journal of Crystal Growth,* vol. 310, pp. 5166-5169, 2008.

[38] J. P. Liu, J. Limb, Z. Lochner, D. Yoo, J.-H. Ryou, and R. D. Dupuis, "Green light-emitting diodes with p-InGaN:Mg grown on c -plane sapphire and GaN substrates," *Physica Status Solidi (a),* vol. 206, pp. 750-753, 2009.

[39] X. A. Cao, J. A. Teetsov, F. Shahedipour-Sandvik, and S. D. Arthur, "Microstructural origin of leakage current in GaN/InGaN light-emitting diodes," *Journal of Crystal Growth,* vol. 264, pp. 172-177, 2004.

[40] X. H. Wu, C. R. Elsass, A. Abare, M. Mack, S. Keller, P. M. Petroff, S. P. DenBaars, J. S. Speck, and S. J. Rosner, "Structural origin of V-defects and correlation with localized excitonic centers in InGaN/GaN multiple quantum wells," *Applied Physics Letters,* vol. 72, pp. 692-694, 1998.

[41] Y. Chen, T. Takeuchi, H. Amano, I. Akasaki, N. Yamada, Y. Kaneko, and S. Y. Wang, "Pit formation in GaInN quantum wells," *Applied Physics Letters,* vol. 72, pp. 710-712, 1998.

[42] S.-N. Lee, J. K. Son, H. S. Paek, Y. J. Sung, K. S. Kim, H. K. Kim, H. Kim, T. Sakong, Y. Park, K. H. Ha, and O. H. Nam, "High-power AlInGaN-based violet laser diodes with InGaN optical confinement layers," *Applied Physics Letters,* vol. 93, p. 091109, 2008.

[43] T. Asano, M. Takeya, T. Tojyo, T. Mizuno, S. Ikeda, K. Shibuya, T. Hino, S. Uchida, and M. Ikeda, "High-power 400-nm-band AlGaInN-based laser diodes with low aspect ratio," *Applied Physics Letters,* vol. 80, pp. 3497-3499, 2002.